Journal of Volcanology and Geothermal Research 481 (2027) 108785

Contents lists available at ScienceDirect

Journal of Volcanology and Geothermal Research

journal homepage: www.journals.elsevier.com/journal-of-volcanology-and-geothermal-research

Phonolite-hosted ultramafic xenoliths from Mayotte (Comores archipelago) and their fluid inclusions record: from mantle evolution to magma ascent and degassing in a trans-lithospheric plumbing system

F. Casetta [a,*], L. Faccincani [b], A.L. Rizzo [c], S. Peres [a], N. Nardini [d], B. Faccini [b], G. Lanzafame [d], M. Liuzzo [e], A. Di Muro [f], M. Prašek [g], L. Mancini [h], M. Masotta [i], F. Colle [j], M. Coltorti [b,e]

[a] Department of Lithospheric Research, University of Vienna, Joseph-Holaubek-Platz 2, UZA II, 1090 Vienna, Austria
[b] Department of Environmental and Prevention Sciences, University of Ferrara, C.so Ercole I D'Este 32, 44121 Ferrara, Italy
[c] Department of Earth and Environmental Sciences, Università degli Studi di Milano-Bicocca, Piazza della Scienza 4, 20126 Milan, Italy
[d] Department of Biological, Geological and Environmental Sciences, University of Catania, Corso Italia 57, 95129 Catania, Italy
[e] Istituto Nazionale di Geofisica e Vulcanologia (INGV) Sezione di Palermo, Via Ugo la Malfa 153, 90146 Palermo, Italy
[f] Laboratoire de Géologie de Lyon: Terre, Planètes, Environnement (LGL-TPE), Université Claude Bernard, Lyon1, 2 Rue Raphaël Dubois, 69622 Villeurbanne Cedex, France
[g] Elettra Sincrotrone Trieste S.C.p.A., SS14 km 163.5 in Area Science Park, 34149 Basovizza, Trieste, Italy
[h] Department of Materials, Slovenian National Building and Civil Engineering Institute (ZAG), Dimičeva Ulica 12, 1000 Ljubljana, Slovenia
[i] Dipartimento di Scienze della Terra, University of Pisa, via S. Maria 53, 56126 Pisa, Italy
[j] Dipartimento di Scienze Chimiche, della Vita e della Sostenibilità Ambientale (SCVSA), Plesso Geologico, University of Parma, Italy

ARTICLE INFO

Keywords:
Fluid inclusions
Phonolite-hosted ultramafic xenoliths
Trans-lithospheric plumbing system
Mayotte (Comores Archipelago)
Lithospheric mantle
X-Ray computed microtomography

ABSTRACT

Combining the geochemistry of gas emissions in active volcanic regions with the signature of mineral-hosted fluid inclusions in deep-derived ultramafic xenoliths can provide important clues on the mobility of fluids through the lithosphere, the ponding/degassing path of magmas underneath active volcanoes and the nature of the underlying mantle. In the Comores archipelago (western Indian Ocean), volcanic activity characterizes the islands located at the NW and SE ends of the archipelago, i.e., Grande Comore (La Grille and Karthala volcanoes, which last erupted in 2007) and Mayotte, where, on 2018–2021, one of the largest submarine eruptions ever documented produced the Fani Maoré cone and lava field. In this study, new mineral and fluid inclusion chemistry data on a unique suite of ultramafic xenoliths brought to the surface by Pleistocene-Holocene phonolites at Petite Terre (Mayotte) were used to shed light on the nature of the lithospheric mantle beneath the Comores archipelago and to investigate the processes responsible for magma ponding and differentiation in a trans-lithospheric plumbing system. We show that ultramafic xenoliths represent a cold and refractory lithospheric mantle beneath Mayotte which, differently from the mantle beneath Grande Comore island, has not been metasomatised by the infiltration of alkaline-carbonatitic melts or fluids. The He-Ne isotopic ratios of mineral-hosted fluid inclusions in Mayotte xenoliths suggest a SCLM-MORB-like nature of the lithospheric mantle beneath the Comores archipelago and overlap with the signature of both mineral-hosted fluid inclusions and surface gas emissions at La Grille and Karthala volcanoes (Grande Comore island). At the same time, anomalously high $^4He/^{40}Ar^*$ and He/CO_2 ratios of the dominantly secondary fluid inclusion trails in Mayotte mantle xenoliths entail the entrapment of fluids during degassing of the host phonolite magma. Combining our data with mineral-based *T-P* estimates, our data suggest that: i) basanite magmas erupted at Fani Maoré in 2018–2021 and the xenoliths-bearing phonolites erupted at Petite Terre followed different *T-P* and degassing paths during ascent to the surface; ii) rapidly ascending phonolite magmas producing explosive volcanism at Mayotte during Pleistocene-Holocene could have formed already at *P* of 0.7–1.0 GPa or even deeper, in a mature trans-lithospheric plumbing system.

* Corresponding author.
E-mail address: federico.casetta@univie.ac.at (F. Casetta).

https://doi.org/10.1016/j.jvolgeores.2026.108785
Received 18 May 2026; Received in revised form 16 November 2026; Accepted 18 November 2026
Available online 23 November 2026
0377-0273/© 2026 The Authors. Published by Elsevier B.V. This is an open access article under the CC BY license (http://creativecommons.org/licenses/by/4.0/).

1. Introduction

Fluid inclusions entrained in ultramafic xenoliths and magmatic phenocrysts formed at crustal to mantle depth provide clues on the evolution of the lithosphere and the deep circulation of volatiles, enabling the investigation of both regional volcanic processes and large-scale geodynamic events (Rizzo et al., 2021; Wieser et al., 2025). Typically, fluid inclusions hosted within olivine and clinopyroxene phenocrysts in lavas or tephra preserve evidence of the evolution of magmatic fluids, allowing tracing the depth of magma genesis, ponding and evolution, the architecture of volcanic plumbing systems (Boudoire et al., 2018; Zanon et al., 2023; DeVitre et al., 2024) and the volatiles exsolution and degassing pattern of melts from their source mantle to the surface (Sandoval-Velasquez et al., 2023a; Lo Forte et al., 2024). Instead, fluid inclusions hosted in minerals in mantle xenoliths bear witness of the volatiles storage and transport at depth, i.e., the nature and amount of volatiles ingassed in, and outgassed from, the lithosphere. This enables to access information about the geodynamic evolution of specific mantle domains, metasomatic processes, and the deepest portions of plumbing systems (Gautheron and Moreira, 2002; Day et al., 2015; Rizzo et al., 2018, 2021; Sandoval-Velasquez et al., 2023b; Yamamoto and Kurz, 2023).

In active volcanic areas, combining the study of fluid inclusions hosted in phenocrysts and/or mantle-derived xenoliths with the characterization of surface gas emissions represents a key frontier in volcano monitoring and geodynamics. This integrated approach allows tracing the evolution of fluids across the entire lithosphere and provides unique constraints on the architecture of volcanic plumbing systems, which traditionally develop at crustal levels, extending from sub-surface to sub-Moho depths (Cashman et al., 2017). However, increasing

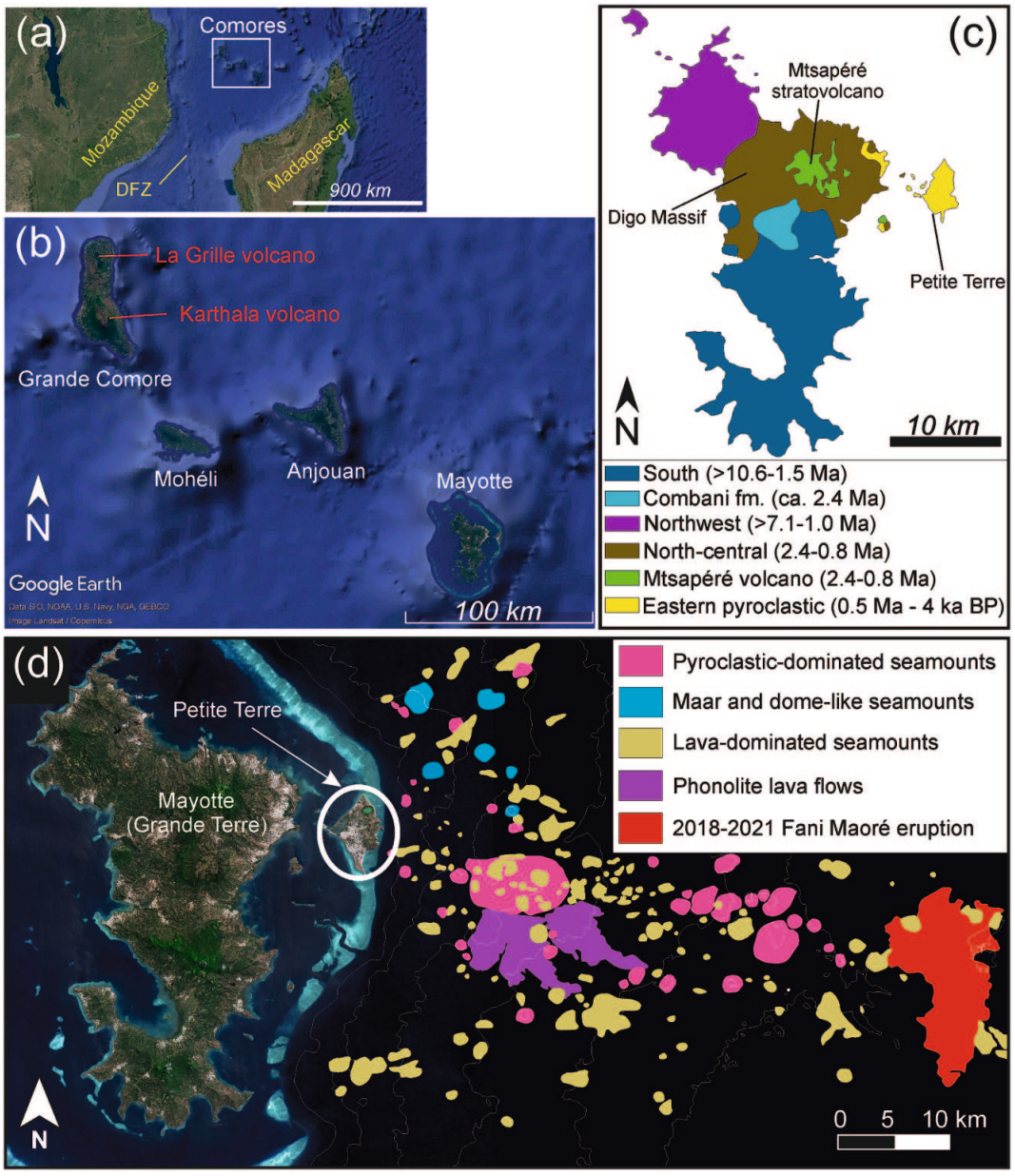

Fig. 1. (a) Location of the Comores archipelago in the Mozambique channel. DFZ = Davie Fracture Zone. Base image source: Google Earth. (b) The Comores archipelago, composed of the islands of Grande Comore, Mohéli, Anjouan and Mayotte (from NW to SE). Base image source: Landsat-Copernicus - Google Earth. (c) Simplified geological map of the island of Mayotte and Petite Terre (modified from Pelleter et al., 2014 – see text for details). (d) Map of the active volcanic ridge East of the Mayotte island showing the location of seamounts, phonolite lava flows and the 2018–2021 Fani Maoré eruption (modified from Berthod et al., 2021a, 2021b; Lacombe et al., 2024). The provenance of the ultramafic xenoliths (Petite Terre) is indicated by a white circle. Base image source: Copernicus Sentinel-2.

geophysical, petrological and geochemical evidence indicates that, in many oceanic intraplate settings, where the crust is relatively thin, plumbing systems extend much deeper, involving trans-lithospheric pathways and magma storage zones within the lithospheric mantle, or even down to the lithosphere-asthenosphere boundary (LAB) (Boudoire et al., 2018; Feuillet et al., 2021; Lo Forte et al., 2024). In such vertically developed systems, magma ponding, crystallization and degassing might occur at multiple depths, and so the fluid inclusions record in both phenocrysts and mantle xenoliths can be either mixed or totally overprinted. Typically, even when preserving the original mantle signature in their noble gas chemistry, fluid inclusions in ultramafic xenoliths can undergo significant re-equilibration in proximity of the Moho or at mid-crustal depth, and thus concomitantly bear a shallow magmatic CO_2 signature (Boudoire et al., 2021; Zanon et al., 2023; Lo Forte et al., 2024; Wieser et al., 2025). Therefore, only a comprehensive record of volatiles in mantle-derived xenoliths, and deep (phenocrysts) to shallow (surface gas emissions) volcanic products, combined with petrological/textural evidence, can provide insights on the overall architecture and dynamics of plumbing systems. To reconstruct the evolution of the lithospheric mantle and track the fluid circulation within active magma plumbing systems in oceanic settings, we present here a petrological and geochemical study of ultramafic xenoliths and their fluid inclusions from the island of Mayotte (Comores archipelago, western Indian Ocean; Fig. 1). Ultramafic xenoliths from Mayotte are ideal study objects to investigate both plumbing system processes and the geodynamic evolution of the Comores archipelago. This because Mayotte is renowned for its high levels of recent volcanic activity, which led to the submarine eruption of Fani Maoré in 2018–2020 (Bachèlery and Hémond, 2016; Famin et al., 2020; Lemoine et al., 2020; Berthod et al., 2021a), and lies at the SE end of the Comores archipelago, whose origin by mantle plume vs. passive lithospheric upwelling is still undisclosed (e.g., Nougier et al., 1986; Class et al., 1998). Deepening the knowledge of the nature and evolution of the volcanism at Mayotte is therefore critical to both understand the regional geodynamics and assess the hazard associated to the recent volcanic and seismic activity. By using mineral chemistry, thermobarometry, fluid inclusions chemistry and synchrotron radiation computed microtomography (SR-μCT) investigations in mantle-derived xenoliths brought to the surface by phonolitic magmas at Mayotte (Fig. 1), we document how mantle and magmatic fluids leave markedly distinct fingerprints on the fluid inclusions record. Through comparison with the chemistry of surface gases and mineral-hosted fluid inclusions from the nearby Grande Comore island (Fig. 1), we provide new insights on the geodynamic evolution of the Comores archipelago, the ascent path of magmas through the lithosphere and the genesis of phonolites beneath Mayotte island.

2. Geological and geodynamic setting

The Comores archipelago comprises four main islands, named Grande Comore, Mohéli, Anjouan, and Mayotte (Fig. 1a-b). Grande Comore island, located at the NW end of the archipelago, hosts the active Karthala volcano, which last erupted in 2007, together with two other volcanic massifs: the old and inactive M'Badjini to the south, and the La Grille volcano to the north, which last erupted in 1029–1424 CE (Bachèlery and Hémond, 2016). The eruptive products from Karthala and M'Badjini volcanoes are generally alkali basalts, while those from La Grille range from basanites to olivine nephelinites (Class et al., 1998). On the island of Grande Comore, mantle xenoliths are hosted within basanite lava flows at Gula Ivoini, on the NE coast (see Coltorti et al., 1999).

At the opposite end of the Comores archipelago rises the island of Mayotte, constituted by Grande Terre and the small islet of Petite Terre, which represents the emerged portions of a ~ 50-km-long volcanic ridge extending eastwards along the eastern flank of the main island of Mayotte (Fig. 1d). the Mayotte volcanic system is completed by multiple maar-, dome-like and lava-dominated seamounts on the eastern side of the island (Fig. 1c-d). In terms of magma composition, Mayotte exhibits the largest variability, from melilitite to phonolite (Bachèlery and Hémond, 2016). Volcanologically, the island can be subdivided into four domains (Fig. 1c; see Pelleter et al., 2014):

- the southern part (from >10.6 to 1.5 Ma) is composed of alkali basalt, basanite and nephelinite lava flows emitted during the main building stage (>10.6–3.0 Ma). These lava flows are intruded by scattered phonolite protrusions, associated to nephelinite/phonolite lava flows and pyroclastic density currents (3.9–3.1 Ma). The last event was the emplacement of basanite/nephelinite lava flows (ca. 2.0–1.5 Ma). The tephriphonolitic/phonolitic Combani massif (ca. 2.4 Ma) is part of the southern domain;
- the Northwest domain (from >7.1 to 1.0 Ma) is constituted by basaltic/basanitic lava flows emitted during a shield building stage, followed by the emplacement of extension-related mafic magmatism, which includes scattered melilitite lava flows and then by the onset of phonolitic domes (3.3–2.5 Ma);
- the North-central sector (from 2.4 to 0.8 Ma) is composed of the basaltic-tephritic lava flows belonging to the Digo massif and by basaltic–tephritic lava flows intruded by phonolitic protrusions belonging to the Mtsapéré stratovolcano;
- the eastern sector (from 0.5 Ma to 4 ka B.P.) represents a recent explosive complex constituted by tuff rings and cones built by phreatomagmatic and strombolian eruptions along the east coast of Grande Terre and in Petite Terre (Pelleter et al., 2014).

From 2018 to 2021, the onset of a large submarine eruption led to the extrusion of >6.5 km^3 basanitic and phonolitic lavas and the genesis of a new 820 m tall edifice, named Fani Maoré (Fig. 1d). Fani Maoré is located at the distal tip of the volcanic ridge departing from Petite Terre and continuing through the Horse-Shoe caldera, typified by bimodal sodic alkaline basanitic-phonolitic magmatism (Fig. 1d) (Berthod et al., 2021a, 2021b; Feuillet et al., 2021; Chauvel et al., 2024; Lacombe et al., 2024). The studied Mayotte ultramafic xenoliths are sampled at Petite Terre, which represents a subaerial expression of this volcanic ridge, and are hosted within recent (Pleistocene-Holocene) phonolite pyroclastics at La Vigie (Fig. 2a-b) (Lacombe et al., 2024). The Mayotte phonolites are generally crystal-poor (<10% phenocrysts) and display a trachytic texture, with feldspar crystals larger than olivine and oxide crystals. Glasses from Petite Terre phonolites exhibit higher alkali contents than phonolites recovered from offshore dredging. Both subaerial and offshore phonolites contain scattered ultramafic xenoliths. Subaerial phonolites are largely degassed, whereas offshore samples retain measurable amounts of dissolved water, reaching up to 1.8 wt% H_2O (Thivet et al., 2023a, 2023b; Le Losq et al., 2026). Subaqueous phonolitic glasses are also characterized by low S concentrations (50–115 ppm) and high halogen contents (Cl = 1492–2301 ppm; F = 1678–2234 ppm), typical of alkaline magmatic systems (Le Losq et al., 2026).

The architecture and degree of maturation of the plumbing system beneath Mayotte, and the location of the main ponding zones where basanites and/or phonolites are produced are still matter of debate, which impact on the assessment of the volcanic hazard in the area. The Moho beneath the main island of Mayotte and Petite Terre is located at a depth of ca. 15–17 km, while the crust beneath the easternmost tip of the volcanic ridge, where the Fani Maoré eruption took place, is thinner (ca. 10–12 km) (Dofal et al., 2018; Feuillet et al., 2021). The depth of the LAB beneath the Mayotte volcanic system is ca. 70 km (Mazzullo et al., 2017; Barruol et al., 2019). Based on melt inclusion analyses and MELTS modelling, the parental melts of the Mayotte-Petite Terre-Fani Maoré magma suite are basanites yielding a pre-eruptive H_2O content of 1.2–2.3 wt% (Berthod et al., 2021a, 2021b), and are thought to originate from partial melting of a carbonated, volatile-enriched mantle source (Chauvel et al., 2024). The deepest ponding zone of basanites is located at the LAB (Feuillet et al., 2021). Berthod et al. (2021a) proposed that

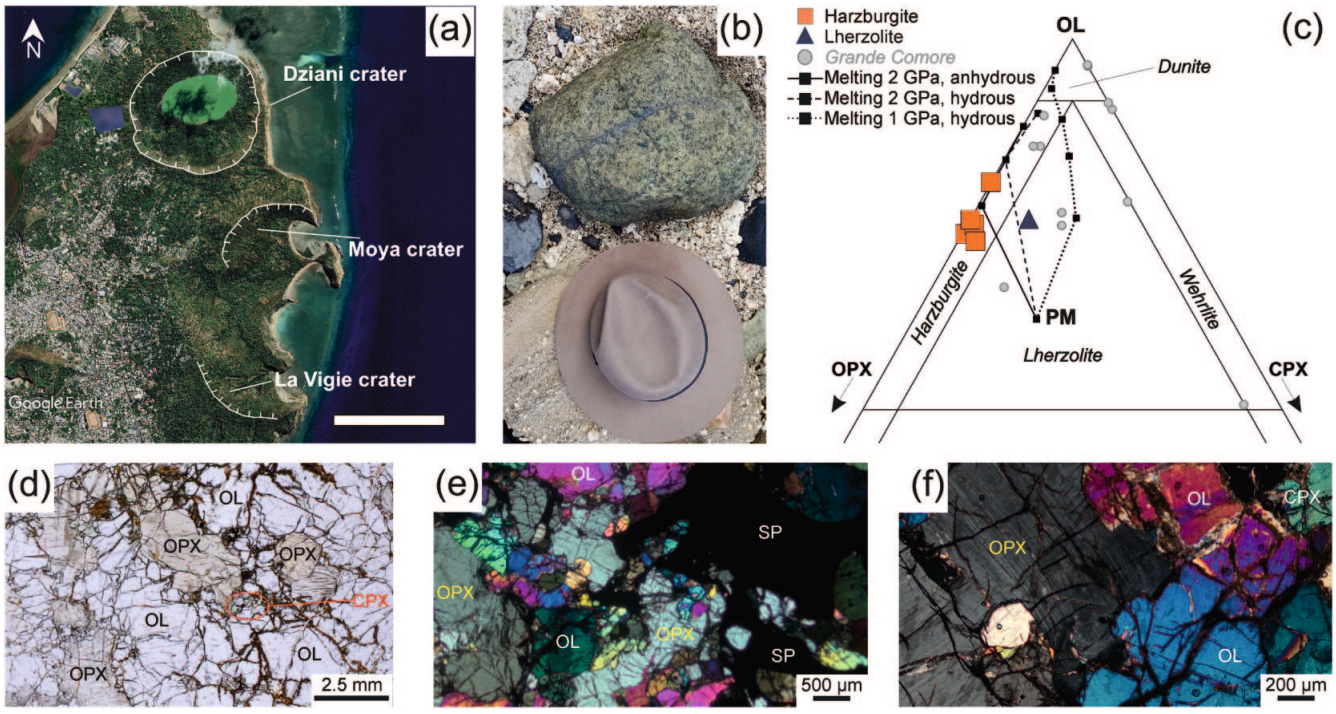

Fig. 2. (a) The easter coast of Petite Terre island, with the Dziani, Moya and La Vigie craters formed by phonolitic explosive volcanism (see Lacombe et al., 2024). Base image source: Landsat-Copernicus - Google Earth. (b) Large peridotite xenolith at La Vigie beach (scale indicated by hat for comparison) (from Lacombe et al., 2024). (c) Ternary diagram for ultramafic rocks showing the modal composition of the studied peridotite xenoliths from Petite Terre (Mayotte) compared to those from the neighbouring Grande Comore (Ventura Bordenca et al., 2023). Melting trends of peridotites in the spinel stability field starting from a Primitive Mantle (PM) composition (solid line = anhydrous melting at 2 GPa; dashed line = hydrous melting at 2 GPa; dotted line = hydrous melting at 1 GPa) are also reported (from Johnson, 1998). (c) Thin section HD scan of an harzburgite mantle xenoliths from Petite Terre. (d-e) Photomicrographs (cross-polarized light) showing the protogranular to slightly porphyroclastic texture (Mercier and Nicolas, 1975) of the studied xenoliths. Ol = olivine; Opx = orthopyroxene; Cpx = clinopyroxene.

phonolitic melts form via ca. 80% fractional crystallization of an assemblage made of clinopyroxene, anorthoclase, magnetite, olivine, apatite and ilmenite, from a starting hydrous basanitic magmas under reduced conditions (ΔFMQ −1), potentially within sub-crustal reservoirs close to the Moho. Subsequent experimental investigations by Andújar et al. (2023) showed that phonolitic residual liquids can also be generated through extensive fractional crystallization at crustal levels, highlighting the importance of pressure in controlling the Fe content of the resulting melts and suggesting relatively shallow production and storage conditions for the Fe-rich submarine phonolites. Passive tomography studies showed that low-velocity zones are located beneath the Petite Terre - Horse-Shoe at a depth of 25–50 km (Foix et al., 2021), in correspondence with the depth of the seismic events recorded during the 2018–2020 eruptive crisis (Mercury et al., 2022). Magnetotelluric investigations identified the occurrence of two conductors beneath the Mayotte-Petite Terre area: a deeper, horizontally extended Conductor C1, located at 25 km depth and interpreted as a mush hosting 22–42% of evolved basanite melt, and a shallower small Conductor C2, located in proximity of the Moho (15–20 km depth) and interpreted as a reservoir hosting 7–10% of phonolite melt (Wawrzyniak et al., 2025). At a regional scale, the origin of the Comores volcanism is also still undisclosed, being attributed either to the migration of the lithosphere over a relatively stable mantle plume (e.g., Emerick and Duncan, 1982; Class et al., 1998) or to passive lithospheric upwelling caused by the reactivation of a very slowly spreading ridge or lithospheric transform zones (e.g., Nougier et al., 1986), the two hypotheses being not mutually exclusive.

3. Samples and methods

A total of n. 12 ultramafic xenoliths hosted within phonolitic tephra deposits at La Vigie (Petite Terre, Fig. 2a-b) were collected during field campaigns in 2018–2019. After a selection based on freshness and size, n. 6 out of 12 xenoliths were prepared as polished thin sections (60 µm in thickness) to determine their textural and mineral chemical features. N. 8 out of 12 xenoliths were also crushed and sieved to separate aliquots of olivine, orthopyroxene and clinopyroxene, which were then characterized in terms of major element chemistry, and used to determine the chemistry of mineral-hosted fluid inclusions. On 2 selected xenoliths, SR-µCT investigations were also performed on separate aliquots of olivine, orthopyroxene and clinopyroxene.

3.1. Mineral major and trace element chemistry

The major element compositions of mineral phases in thin sections were determined by Electron Probe Micro Analysis (EPMA) using a Cameca SXFive FE electron microprobe equipped with five wavelength-dispersive (WD) and one energy-dispersive (ED) spectrometers hosted at the Core Facility Electron Beam Microanalysis (CFE), University of Vienna (Austria). Routine analyses of olivine, orthopyroxene, clinopyroxene and spinel were performed using 15-kV accelerating voltage, 20 nA beam current, 20 s counting time at the peak position, 1 µm beam spot. Limits of detection (LOD) were: 100–250 ppm for Al, Na, Cr, Mn and Ti; 300–500 ppm for Si, Fe, Mg, Ca, Ni and K. Natural and synthetic standards were used for calibration. The PAP routine was applied for matrix correction of all analyses (Pouchou and Pichoir, 1991). The composition of minerals in separated aliquots was also determined by Electron Probe Micro Analysis (EPMA) using a JEOL JXA-8200 at the Bayerisches Geoinstitut of the University of Bayreuth (Germany), adopting the same analytical conditions and standards for calibration.

Trace element analyses of olivine, clinopyroxene and orthopyroxene were carried out on thin sections using a laser ablation-inductively coupled plasma-mass spectrometry (LA-ICP-MS) system installed at the Centre for Instrument Sharing of University of Pisa (CISUP). The

system is composed by an Elemental Scientific NWR-193 (ArF) excimer laser equipped with a TwoVol2 two-volume cell, coupled with a PerkinElmer NexION 2000 ICP-MS. The laser was operated at a repetition rate of 10 Hz, using a fluence of 2.7 J/cm^2 and a spot size of 80 μm. Helium was used as gas carrier, with a flow rate of 700 mL/min. The ICP-MS was operated with a RF power of 1300 W and with a flow rate of the Ar nebulizer of 900 mL/min. A total of n. 36 masses were collected, using a dwell time of 8 ms and a total sweep time of 0.430 s. Signals were acquired for 30 s during ablation and 50 s with laser off (background). The synthetic glass standard NIST612 was used for tuning of the ICP-MS and as calibration standard, whereas the synthetic glass standard NIST610 and the natural MPI standard StHs/80 as quality monitor. Standard glasses were measured every 6–8 spots. The Ca concentration (measured by EPMA) was used as internal standard for clinopyroxene, while Si for orthopyroxene and olivine. Precision was better than 6% for all the elements, except for Ti (~12%). The LOD was calculated according to Howell et al. (2013). Data processing was conducted using the commercial software Iolite v4 (Paton et al., 2011).

3.2. Fluid inclusions chemistry

After crushing and sieving of 8 samples, 26 aliquots of pure, unaltered olivine (8 + 1 replicate), orthopyroxene (7 + 6 replicates) and clinopyroxene (3 + 1 replicate) were handpicked for performing noble gases (He, Ne, Ar) and CO_2 analyses in fluid inclusions at the noble gas isotopes laboratory of INGV-Palermo, Italy (see Rizzo et al., 2018, 2021). Mineral aliquots were cleaned ultrasonically in 6.5% HNO_3 for noble gas and in 6.5% HCl for CO_2 measurements, before being rinsed with deionised water and acetone in an ultrasonic bath. Aliquots were weighed and loaded into an ultra-high-vacuum (UHV) crusher system, which was pumped and baked for 48 h to reach UHV conditions. Fluid inclusions were released by single-step crushing at a pressure of ca. 200 bar and room temperature. The CO_2 estimation was first performed during noble gas extraction at the time of crushing, by quantifying the total gas pressure ($CO_2 + N_2 + O_2 +$ noble gases) and subtracting the residual pressure of $N_2 + O_2 +$ noble gases after removing CO_2 using a "cold finger" immersed in liquid N_2 at ~196 °C. After CO_2 removal, the gas mixture was purified using Zr—Al getter pumps in a stainless-steel UHV preparation line to remove all gas species (N_2, H_2, H_2O) except noble gases. Then, Ar was removed in a cold finger with active charcoal immersed in liquid nitrogen, while He and Ne were adsorbed in a cold head with active charcoal cooled at 10 K and then moved at 40 and 80 K in order to release first He and then Ne. The He-Ne isotopes were analysed using two different split-flight-tube Noble Gas Mass Spectrometers (Helix SFT Thermo), while Ar isotopes were quantified by a multicollector mass spectrometer (Argus, GVI).

3.3. Synchrotron radiation computed microtomography (SR-μCT) measurements and image analysis

Single crystals of olivine, orthopyroxene and clinopyroxene separates from 2 representative samples (between 9 and 20 crystals per separate, for a total of 6 separates) were selected to perform three-dimensional (3D) textural and volumetric characterization of fluid inclusions by means of SR-μCT measurements in propagation-based phase-contrast mode (Polacci et al., 2010; Baker et al., 2012) at the SYRMEP beamline of the Elettra Sincrotrone Trieste laboratory (Basovizza - Trieste, Italy). Acquisitions were performed in filtered white beam configuration with a polychromatic spectrum and a filter of 1.5 mm Si plus 1.0 mm Al (27 keV energy). The detector used was an air-cooled, 16 bit, 2048 × 2048-pixels, sCMOS macroscope camera (Hamamatsu C11440-22C) lens-coupled to a 17 μm-thick LSO:Eu scintillator screen. In order to better identify μm-sized objects like intra-crystalline fluid inclusion trails, the effective pixel size of the detector was set to 0.9 × 0.9 μm^2, yielding a maximum field of view of ~1.8 × 1.8 mm^2. Scans were acquired in local or region-of-interest mode, setting the sample-to-detector propagation distance to 100 mm. This led to an increase in the visibility of the different features present in the samples, thanks to an edge-enhancement effect at their borders (Mancini et al., 1998). For each sample, a set of 1800 radiographs (projections) of the sample over a 180° angular rotation was recorded with an exposure time/projection of 500 ms.

Reconstruction of the 3D tomographic images was done with the Syrmep Tomo Project (STP) software suite (Brun et al., 2015), applying, before the reconstruction, a single-distance phase-retrieval algorithm based on the transport of intensity equation (Paganin et al., 2002) to the acquired projections. Combining phase-retrieval with a filtered back-projection tomographic reconstruction algorithm (Herman, 1980), the 3D distribution of the refraction index in the xenoliths was obtained. After ad-hoc optimization, a value of 30 was chosen for the $\delta/\beta = \gamma$ parameter (ratio between the real and imaginary parts of the complex refractive index). The selected value allowed to enhance the contrast between the different features in the imaged crystalline phases, keeping the blurring effects of phase-retrieval processing as low as possible. The reconstructed slices (stacks of 16-bit images in TIF format) were imported into the open-source software Fiji (Schindelin et al., 2012). A 3D thresholding was applied to segment vesicles, fluid inclusions and mineral grains, which were assigned to separate volumes of interest (VOIs). Threshold values were determined from grey-level histograms by identifying the minimum between the grains and the vesicle signal peaks and were consistently applied across samples, with minor adjustments to account for intensity variability. The resulting segmented volumes were manually refined using Dragonfly software (Dragonfly, version 2020.2; Object Research Systems (ORS) Inc., Montreal, Canada). Vesicles and fluid inclusions connected to the exterior of the grains were manually identified and removed. Vesicles smaller than 4 voxels (2.916 μm^3) were excluded from the total volume estimate. The total volumes of the different crystal phases and of voids/fluid inclusions were extracted as absolute volume measurements (see Lanzafame et al., 2025). Individual grains for each crystal phase, together with their internal voids and fluid inclusions, were isolated and 3D rendered to allow the visualization of fluid inclusions within the grains.

4. Results

4.1. Petrography and mineral chemistry

The studied ultramafic xenoliths are classified as n. 9 harzburgites, n. 2 clinopyroxene-poor lherzolites (samples MAY101126-67 and May11-4a) and n. 1 wehrlite (sample May106) (Fig. 2c). The dominant presence of harzburgite xenoliths was also reported at La Vigie by Berthod et al. (2021b). Harzburgites and lherzolites are coarse- to medium-grained and have protogranular to slightly porphyroclastic texture (Fig. 2d-f). They are composed of primary olivine with $Fo_{90.5–91.8}$ and NiO = 0.35–0.46 wt%, and Cr-rich spinel (Cr# = 38–57) (Fig. 3a-b). A similar Fo range ($Fo_{90.2–91.9}$) for primary olivine cores in harzburgites was reported by Berthod et al. (2021b). Primary orthopyroxene has Mg# 91–92, Al_2O_3 = 1.7–2.9 wt% and Cr_2O_3 = 0.5–0.9 wt%, overlapping the composition of primary orthopyroxene in the harzburgite xenoliths reported by Berthod et al. (2021b) (Mg# 91, Al_2O_3 = 1.6–2.5 wt% and Cr_2O_3 = 0.3–0.7 wt%) (Fig. 3c). Primary clinopyroxene has Mg# 92–94, Al_2O_3 = 2.5–3.6 wt% and Cr_2O_3 = 0.8–1.5 wt%, being also comparable to primary clinopyroxene in the harzburgites reported by Berthod et al. (2021b) (Mg# 92–94, Al_2O_3 = 1.8–3.4 wt% and Cr_2O_3 = 0.6–1.3 wt%) (Fig. 3d). Local neoblastic assemblages are usually found at the edges of orthopyroxene (Fig. 2e), and contain secondary olivine ($Fo_{90–93}$, NiO = 0.33–0.50 wt%; Fig. 3a), clinopyroxene (Mg# 91–94, Al_2O_3 = 1.9–3.6 wt%; Fig. 3d) and spinel. The wehrlite sample May106 has cumulate texture and an overall Fe-rich chemistry, consistent with its cumulate origin: it contains $Fo_{84–85}$ and Ni-poor (0.18–0.21 wt%) olivine and clinopyroxene with Mg# = 85–86, Al_2O_3 = 4.1–5.0 wt% and TiO_2 = 0.9–1.3 wt% (Fig. 3a-d).

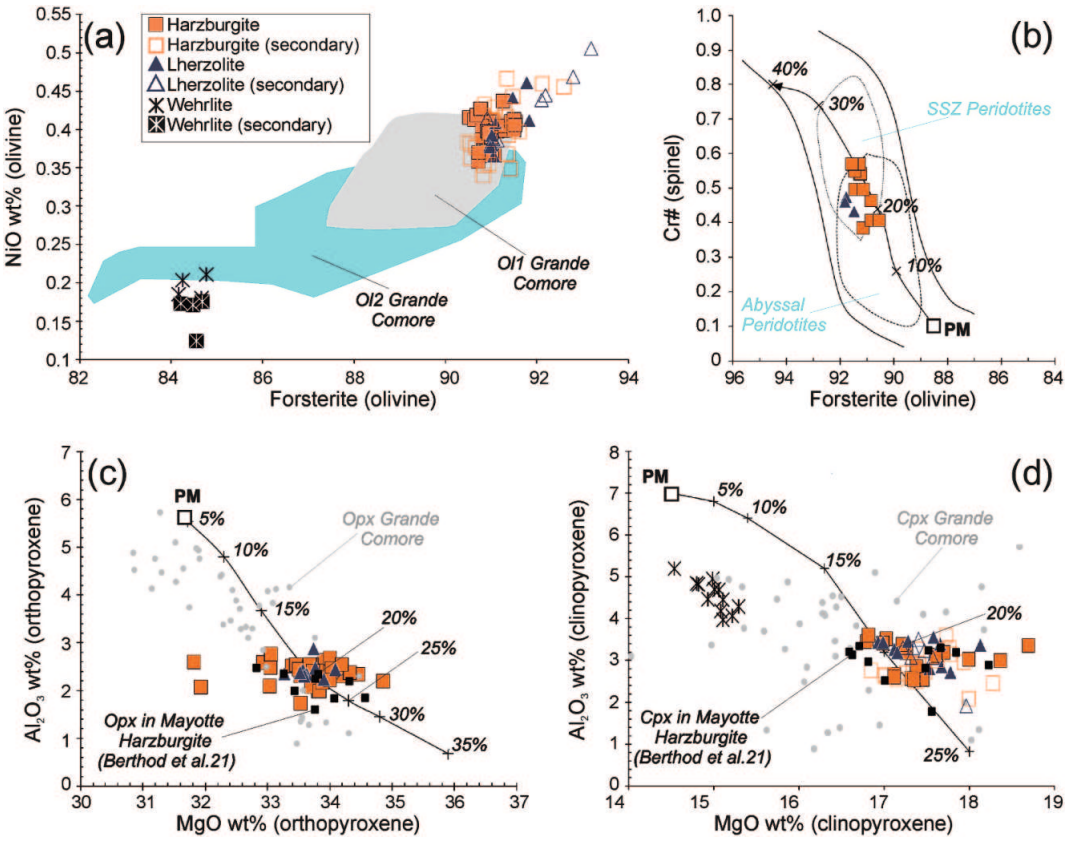

Fig. 3. Mineral major element chemistry in the studied ultramafic xenoliths from Petite Terre (Mayotte) (our study and Berthod et al., 2021b) in comparison to those from Grande Comore mantle xenoliths (Ventura Bordenca et al., 2023). (a) NiO (wt%) vs. Forsterite content of olivine. (b) Olivine-Spinel Mantle Array (OSMA) diagram (Arai, 1994) showing the Cr# in spinel vs. Fo content of olivine. The composition of the olivine-spinel pair in the Primitive Mantle (PM) was calculated as in Rizzo et al. (2021). The black arrow refers to the melting model of Arai (1994); numbers and thick marks correspond to melt extracted percentages. Compositional fields of Supra-Subduction Zone (SSZ; Pearce et al., 2000) and Abyssal Peridotites (Dick and Bullen, 1984) are also shown for comparison. (c) Al_2O_3 (wt%) vs. MgO (wt%) content of orthopyroxene. (d) Al_2O_3 (wt%) vs. MgO (wt%) content of clinopyroxene. The melting curves in (c) and (d) are developed as in Upton et al. (2011) and Melchiorre et al. (2020) and represent the composition of orthopyroxene and clinopyroxene after peridotite melting in the spinel stability field (1–2 GPa). Numbers and thick marks correspond to melt extracted percentages. In (c) and (d), small black squares represent the composition of orthopyroxene and clinopyroxene in Mayotte harzburgite xenoliths from Berthod et al. (2021b).

In both harzburgites and lherzolites, pyroxenes are generally depleted in all trace elements. The chondrite-normalized (Sun and McDonough, 1989) Rare Earth Element (REE) patterns of clinopyroxene are typified by LREE-MREE depletion, with occasional slight enrichment in La, and have HREE contents lying at around 1.5 x chondritic (Fig. 4a). An exception is one harzburgite sample (sample MAY101120–65), in which clinopyroxene exhibits a relatively flat REE pattern at elemental concentrations of ca. 1–1.5 x chondritic (Fig. 4a). Orthopyroxene has HREE content of 0.2–1.0 x chondritic, and LREE-MREE values ranging from b.d.l. to 0.04 x chondritic (Fig. 3b). Olivine trace element distribution is consistent with that of refractory spinel-bearing peridotites in terms of Ca, Al, Cr, Ti and V/Sc distribution (Fig. 4c-e; Casetta et al., 2025). On average, olivine in lherzolite is relatively enriched in Cr (58–105 ppm), Ca (279–356 ppm) and Al (44–79 ppm) with respect to olivine in harzburgites (Cr = 23–85 ppm; Ca = 129–349 ppm; Al = 15–51 ppm) (Fig. 4c-e), at comparable Ti content (2–5 ppm) and V/Sc ratio (0.5–0.9) (Fig. 4c-e). No hydrous phases were identified in the studied xenoliths. All mineral chemistry data are reported in Tables 1 and S1-S7.

4.2. Fluid inclusions chemistry

Mineral-hosted fluid inclusions are dominated by CO_2, whose concentration ranges from 2.5×10^{-10} to 4.6×10^{-7} mol/$g_{(sample)}$, followed by N_2* (1.1×10^{-10} to 1.0×10^{-8} mol/$g_{(sample)}$), and then noble gases (Table 2). Within the same sample, orthopyroxene and clinopyroxene generally release more gas than olivine, in agreement with data from mantle xenoliths suites from continental (e.g., Rizzo et al., 2018, 2021; Faccini et al., 2020; Casetta et al., 2022) and oceanic (Sandoval-Velasquez et al., 2023a, 2023b) settings.

Among noble gases, the concentration of ^{4}He and ^{3}He ranges from 1.1×10^{-13} to 6.9×10^{-11} mol/$g_{(sample)}$ and from 9.8×10^{-19} to 5.5×10^{-16} mol/$g_{(sample)}$, respectively. The content of ^{40}Ar* ranges from 4.9×10^{-14} to 3.1×10^{-11} mol/$g_{(sample)}$, and the abundance of ^{20}Ne* is 1.4×10^{-15}-2.0×10^{-13} mol/$g_{(sample)}$ (Table 2). The ^{4}He/^{20}Ne ratio is highly variable, ranging from 7 to 1216 in olivine-, and from 6 to 5414 in orthopyroxene- and clinopyroxene-hosted fluid inclusions (Fig. 5a; Table 2). In both olivine- and pyroxene-hosted fluid inclusions, the ^{40}Ar/^{36}Ar ratio ranges between 298 and 2682, with fluid inclusions in the cumulate wehrlite having ^{40}Ar/^{36}Ar of ca. 1520. In all samples, the ^{20}Ne/^{22}Ne ratio is 9.8–10.4 and the ^{21}Ne/^{22}Ne ratio is 0.0287–0.0358 (Table 2). The measured ^{3}He/^{4}He ratios corrected for air contamination (Rc/Ra) in olivine-hosted fluid inclusions are 5.9–6.9 in harzburgites and lherzolites while ~5.7 in the wehrlite cumulate; more in detail, the Rc/Ra values are in the range of 5.9–6.8 in orthopyroxene- and of 6.5–6.7 in clinopyroxene-hosted fluid inclusions in harzburgites and lherzolites (Fig. 5a-b; Table 2). The ^{4}He/^{40}Ar* ratios are quite variable between inclusion sets, varying between 1.3 and 6.0 in olivine- to 0.3–47.4 in orthopyroxene-, and 0.8–19.4 in clinopyroxene-hosted fluid inclusions (Fig. 5b; Table 2). Likewise, the ^{4}He/CO_2 ratio of the

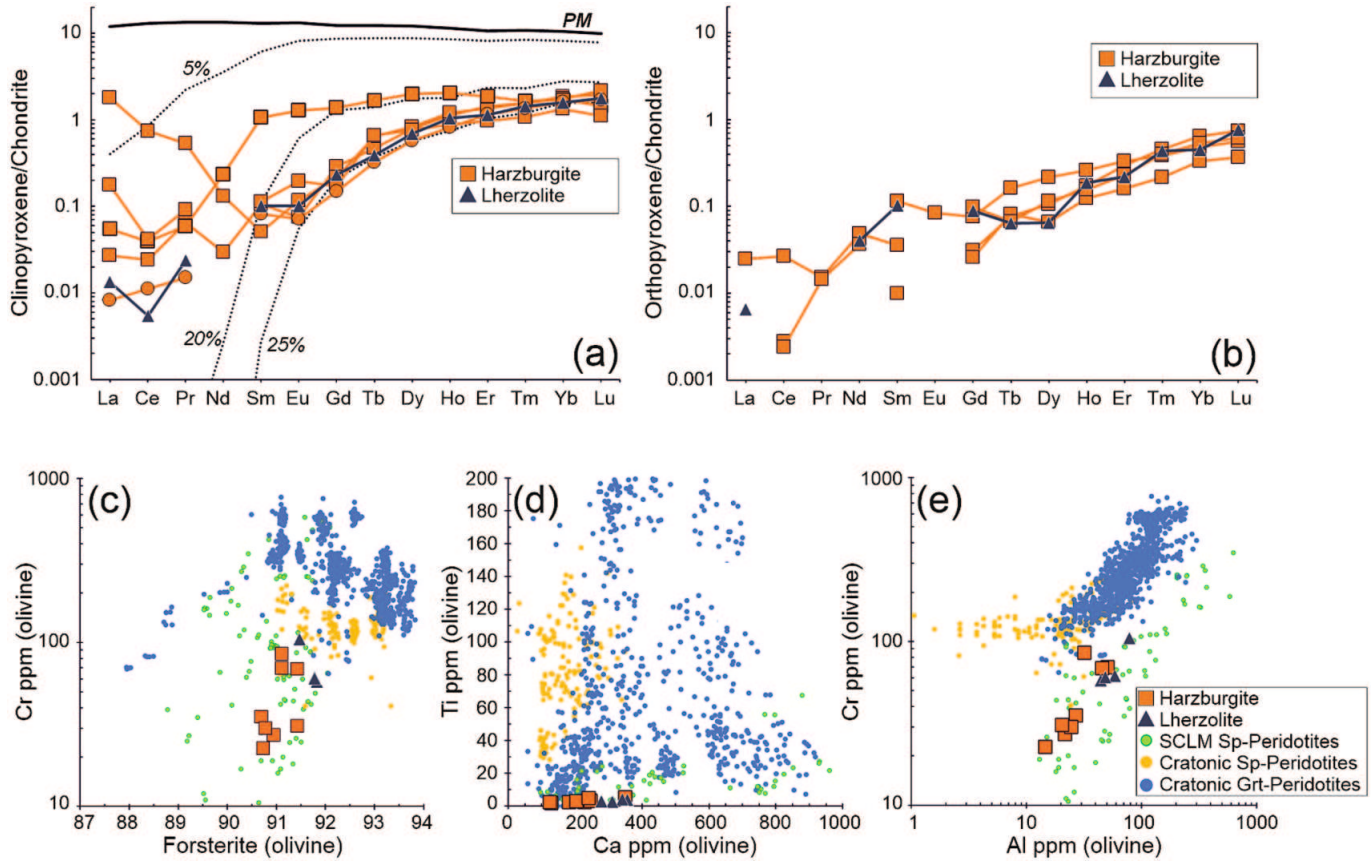

Fig. 4. Mineral trace element chemistry in the studied ultramafic xenoliths from Petite Terre (Mayotte). (a-b) Chondrite-normalized (Sun and McDonough, 1989) average REE patterns of clinopyroxene (a) and orthopyroxene (b) in harzburgites and lherzolite. Dashed lines in (a) represent clinopyroxene REE patterns after 5% to 25% fractional melting starting from clinopyroxene in PM (solid bold line). Modelling parameters: starting PM source = 0.53 Ol, 0.27 Opx, 0.17 Cpx, 0.03 Sp; mineral melting contribution = −0.06 Ol, +0.28 Opx, +0.67 Cpx, +0.11 Sp (Kinzler, 1997; Johnson, 1998). (c-d-e) Cr (ppm) vs. Forsterite, Ti (ppm) vs. Ca (ppm) and Cr (ppm) vs. Al (ppm) content in olivine in the studied harzburgite and lherzolite xenoliths compared to olivine from SCLM spinel-bearing peridotites, cratonic spinel- and garnet-bearing peridotites (Casetta et al., 2025).

inclusions ranges from 4.3×10^{-5} to 6.5×10^{-2}, irrespective of the nature of the host mineral (Table 2).

4.3. The 3D distribution of fluid inclusions

The texture, volume and distribution of fluid inclusions were determined in 1 harzburgite and 1 lherzolite on separates of olivine (28 grains), orthopyroxene (23 grains) and clinopyroxene (18 grains) (Table 3). Following the nomenclature and classification scheme of Roedder (1984) and Andersen and Neumann (2001), fluid inclusions were subdivided into isolated (i.e., primary) and trails (i.e., secondary). The fluid inclusions volume in olivine is almost constant between harzburgite and lherzolite, being 0.10–0.11 vol% (Table 3). Olivine hosts fluid inclusions both as isolated and as trails set in healed fractures planes (i.e., secondary), the latter being volumetrically dominant (Fig. 6, S1, S2). The fluid inclusions volume in orthopyroxene varies significantly between harzburgite (0.04 vol%) and lherzolite (0.16 vol%). Fluid inclusions in orthopyroxene occur mostly as secondary trails in healed cracks, cross-cutting the cleavage plans and the clinopyroxene exsolution lamellae (Fig. 6, S1, S2). Fluid inclusions in clinopyroxene occupy 0.11 vol% in the harzburgite and 0.22 vol% in the lherzolite sample (Table 3), and are rarely isolated, being mostly organized on healed cracks, and aligned with orthopyroxene exsolution lamellae (Fig. 6, S1, S2). Occasionally, the fluid inclusion trails propagate from the small, localized reaction zones at the crystal edges.

5. Modelling and discussion

5.1. A cold and refractory lithospheric mantle beneath Mayotte

Mineral chemistry data indicate that all harzburgite and clinopyroxene-poor lherzolite xenoliths from Mayotte represent fragments of depleted lithospheric mantle, in accordance with what reported by Berthod et al. (2021b). Olivine-spinel pairs fall within the Mantle Array (OSMA), in the upper end of the abyssal peridotites field, and record partial melting degrees of 20–25% (Fig. 3b). In MgO vs. Al_2O_3 diagrams, both orthopyroxene and clinopyroxene lie in proximity of the ideal partial melting curve at 1–2 GPa, confirming that lherzolites and harzburgites experienced ca. 20–22% partial melting (Fig. 3c-d). The HREE patterns of clinopyroxene and orthopyroxene also suggest a re-equilibration after 20–25% partial melting, with no subsequent metasomatic overprint (Fig. 4a-b). An exception is the occasional LREE enrichment, which could be ascribed to the late-stage infiltration of the host melt. The general depletion of olivine in *T*-sensitive (e.g., Al, Cr, Ca) and metasomatism-sensitive (e.g., Ti) (Fig. 4c-e) elements also indicates that the lithospheric mantle beneath Mayotte was not thermo-chemically perturbed by the infiltration of melts/fluids during long-lasting events or at high melt/fluid-rock ratios. This contrasts with the geochemical signature of the lithospheric mantle beneath the neighbouring Grande Comore, where lherzolites and harzburgites record variable degrees of melt extraction, ranging from 5 to 20% to 15–35%, respectively, followed by significant metasomatism (Ventura Bordenca et al., 2023), as testified by their relative Fe-Al enrichment and Mg-Ni-

Table 1

Modal composition, texture, major element chemistry of primary mineral phase constituents (min.-max. range) and *T-P-fO*$_2$ conditions of last equilibrium (with associated standard deviation, StD) recorded by ultramafic xenoliths from Petite Terre - Mayotte. Thermobarometers: B91 = Ballhaus et al. (1991); BKN90 = Brey and Köhler (1990); *P* (geotherm) = pressure extrapolated based on the local geothermal gradient using temperature from B91 as input. *P* (Ca-in-Ol) = pressure calculated by Köhler and Brey (1990) barometer. Oxygen fugacity was calculated relative to the FMQ buffer by means of the Ballhaus et al. (1991) oxybarometer. Lh, lherzolite; Hz, harzburgite; Weh, wehrlite; Ol, olivine; Opx, orthopyroxene; Cpx, clinopyroxene; Sp, spinel. * = *T-P* data for clinopyroxene in cumulate wehrlite sample May106 were calculated using the thermobarometer of Ágreda-López et al. (2024). The analytical methods adopted for each sample are also reported: EPMA = Electron Probe Micro Analysis; LA-ICP-MS = Laser Ablation-Inductively Coupled Plasma-Mass Spectrometry; NGMS + CO_2 = Noble Gas Mass Spectrometer and manometric CO_2 quantification; SR-μCT = Synchrotron radiation computed microtomography.

Sample	Rock type	Texture	Analytical methods	Modal abundances				Ol chemistry		Opx chemistry		Cpx chemistry		Sp chemistry		T-P-*f*O$_2$ conditions								
				Ol	Opx	Cpx	Sp	Fo	NiO (wt %)	Mg#	Al_2O_3 (wt%)	Mg#	Al_2O_3 (wt%)	Mg#	Cr#	T (°C) B91	StD	T (°C) BKN90	StD	P (GPa) geotherm	StD	P (GPa) Ca-in-Ol	StD	log *f*O$_2$ [ΔQFM]	StD
MAY101120-6	Hz	Porphyr.	EPMA, LA-ICP-MS, NGMS+CO_2	68.1	31.0	0.5	0.4	91.1–91.4	0.40	91.4–91.7	2.0–2.5	92.5–93.7	2.5–3.0	62.5	0.50	856	10	922	1	1.8	0.04	2.1	0.3	−0.48	0.05
MAY101120-64	Hz	Protogr.-Porphyr.	EPMA, LA-ICP-MS	70.2	29.0	0.1	0.7	90.5–91.1	0.39–0.42	90.8–91.2	2.5–2.6	92.1–93.1	2.7–3.4	56.0–60.5	0.38–0.46	728	40	937	56	1.4	0.13	–	–	−0.06	0.43
MAY101120-65	Hz	Protogr.-Porphyr.	EPMA, LA-ICP-MS	66.6	30.0	2.5	0.9	91.2–91.5	0.40–0.44	91.5–91.9	1.7–2.1	92.8–93.6	2.5–2.6	54.9–58.2	0.54–0.57	751	37	933	35	1.4	0.12	–	–	−1.24	0.17
MAY101120–66	Hz	Porphyr.	EPMA	76.1	23.0	0.0	0.9	91.5	0.41	91.5–91.9	2.2–2.5	–	–	–	–	–	–	–	–	–	–	–	–	–	–
MAY101126-67	Lh	Porphyr.	EPMA, LA-ICP-MS	68.0	20.0	8.0	4.0	91.5–91.8	0.41–0.46	91.4–91.7	2.2–2.9	92.6–93.4	2.7–3.4	61.7–64.2	0.43–0.47	781	25	901	22	1.5	0.08	1.1	0.3	−0.90	0.16
MAY181215-14	Hz	Protogr.-Porphyr.	EPMA, LA-ICP-MS, NGMS+CO_2, SR-μCT	69.7	29.0	1.0	0.3	90.7–90.9	0.37–0.43	90.9–91.0	2.4–2.8	92.4–93.0	3.4–3.6	–	–	766	39	889	27	1.5	0.00	1.3	0.1	−1.43	0.17
May11-4a	Lh	Mineral separate	EPMA, NGMS+CO_2, SR-μCT	–	–	–	–	91.0–91.1	0.37–0.41	91.1–91.4	2.3–2.5	92.5–92.8	3.4–3.6	–	–	–	–	–	–	–	–	–	–	–	–
May11-4b	Hz	Mineral separate	EPMA, NGMS+CO_2	–	–	–	–	90.6–90.8	0.36–0.41	90.8–91.2	2.2–2.3	–	–	–	–	–	–	–	–	–	–	–	–	–	–
May11-4c	Hz	Mineral separate	EPMA, NGMS+CO_2	–	–	–	–	91.5	0.40–0.41	91.4–91.8	2.2–2.5	–	–	–	–	–	–	–	–	–	–	–	–	–	–
May11-4d	Hz	Mineral separate	EPMA, NGMS+CO_2	–	–	–	–	90.8–91.1	0.36–0.40	91.0–91.3	2.3–2.5	–	–	–	–	–	–	–	–	–	–	–	–	–	–
May11-6a	Hz	Mineral separate	EPMA, NGMS+CO_2	–	–	–	–	90.9–91.0	0.39–0.40	91.0–91.3	2.4–2.6	–	–	–	–	–	–	–	–	–	–	–	–	–	–
May106	Weh	Mineral separate	EPMA, NGMS+CO_2	–	–	–	–	84.2–84.7	0.18–0.21	–	–	84.9–86.1	4.0–5.2	–	–	1162*	7*	–	–	1.1*	0.1*	–	–	–	–

Table 2

Concentration (mol/g) and isotopic compostion of noble gases and CO_2 concentration (mol/g) in mineral-hosted fluid inclusions in ultramafic xenoliths from Petite Terre - Mayotte. Lh, lherzolite; Hz, harzburgite; Weh, wehrlite; Ol, olivine; Opx, orthopyroxene; Cpx, clinopyroxene. For each mineral phase, the average Mg# ($Mg/(Mg + Fe_{TOT})$ mol%) is also indicated. "Air" concentration (mol/g) corresponds to the sum of calculated atmosphere-derived N_2, O_2, and Ar concentrations. Number in brackets after sample name indicate the analytical replicates.

Sample	Rocktype	Mineral	Mg	^4He	^3He	^{20}Ne	^{21}Ne	^{22}Ne	CO_2	N_2*	Air	^{40}Ar	^{36}Ar	^{40}Ar*	$^4He/^{20}Ne$	$^4He/^{40}Ar$*	R/Ra	Rc/Ra	Err Rc/Ra + / −	$^{40}Ar/^{36}Ar$	Err. (%)	$^{38}Ar/^{36}Ar$	Err. (%)	$^{20}Ne/^{22}Ne$	$Err^{20}Ne/^{22}Ne$ + / −	$^{21}Ne/^{22}Ne$	$Err^{21}Ne/^{22}Ne$ + / −	$^3He/^{36}Ar$
MAY 101120-6	Hz	Ol	91.3	3.1E-12	3.0E-17	8.3E-15	2.6E-17	8.4E-16	3.6E-09	–	4.5E-10	6.5E-12	1.4E-14	2.3E-12	371.9	1.33	6.93	6.93	0.08	464.0	0.07	0.1777	0.18	9.97	0.02	0.0302	0.0005	2.10E-03
MAY 181215-14	Hz	Ol	90.8	1.1E-13	9.8E-19	9.4E-15	1.7E-17	5.9E-16	2.7E-10	1.4E-09	3.0E-10	2.8E-12	9.4E-15	–	12.2	–	6.17	6.32	0.16	298.8	0.06	0.1762	0.18	9.89	0.03	0.0292	0.0004	1.04E-04
MAY 181215-14 (2)	Hz	Ol	90.8	1.4E-13	1.3E-18	2.0E-14	3.5E-17	1.2E-15	7.1E-10	–	5.2E-10	4.8E-12	1.6E-14	–	7.4	–	6.09	6.33	0.15	298.2	0.06	0.1765	0.18	9.77	0.02	0.0291	0.0003	7.72E-05
May11-4a	Lh	Ol	91.0	9.1E-12	8.4E-17	2.2E-14	5.1E-17	1.7E-15	9.1E-10	–	2.7E-10	4.0E-12	8.4E-15	1.5E-12	418.0	6.01	6.60	6.61	0.06	479.1	0.07	0.1854	0.18	9.92	0.02	0.0297	0.0003	9.90E-03
May11-4b	Hz	Ol	90.7	1.6E-12	1.5E-17	1.4E-14	3.2E-17	1.1E-15	1.0E-08	2.5E-09	2.9E-10	3.1E-12	9.2E-15	3.9E-13	113.3	3.94	6.90	6.91	0.06	341.2	0.06	0.1859	0.18	9.84	0.02	0.0292	0.0003	1.62E-03
May11-4c	Hz	Ol	91.5	3.3E-12	3.1E-17	1.7E-14	4.0E-17	1.3E-15	1.1E-08	3.4E-09	3.8E-10	6.0E-12	1.2E-14	2.5E-12	195.9	1.32	6.71	6.72	0.06	512.1	0.55	0.1859	0.18	9.96	0.02	0.0300	0.0003	2.61E-03
May11-4d	Hz	Ol	91.0	3.3E-12	3.1E-17	2.6E-14	6.1E-17	2.1E-15	9.2E-09	2.2E-09	4.8E-10	5.6E-12	1.5E-14	1.1E-12	126.3	3.00	6.69	6.71	0.06	370.9	0.71	0.1858	0.18	9.85	0.01	0.0291	0.0002	2.01E-03
May11-6a	Hz	Ol	91.0	1.4E-11	1.3E-16	2.5E-14	5.8E-17	2.0E-15	7.9E-09	2.5E-09	4.5E-10	8.3E-12	1.4E-14	4.1E-12	576.8	3.44	6.53	6.53	0.06	587.6	0.46	0.1908	0.19	9.87	0.01	0.0298	0.0002	8.97E-03
May106	Weh	Ol	84.5	2.0E-11	1.6E-16	1.6E-14	3.3E-17	1.1E-15	4.6E-07	5.7E-09	2.5E-10	1.2E-11	7.9E-15	9.8E-12	1216.4	2.01	5.73	5.73	0.21	1519.7	0.44	0.1661	0.18	10.24	0.02	0.0327	0.0003	1.98E-02
MAY 101120-6	Hz	Opx	91.6	5.1E-11	4.5E-16	1.2E-14	3.8E-17	1.2E-15	1.0E-09	9.4E-10	3.4E-10	5.4E-12	1.1E-14	2.3E-12	4319.0	22.36	6.42	6.42	0.08	514.7	0.09	0.1756	0.18	10.01	0.04	0.0324	0.0007	4.26E-02
MAY 181215–14	Hz	Opx	91.0	2.5E-12	2.2E-17	2.7E-15	4.8E-18	1.8E-16	2.9E-10	1.1E-10	8.7E-11	8.6E-13	2.7E-15	5.7E-14	928.0	44.00	6.49	6.49	0.18	319.1	0.10	0.1727	0.18	9.95	0.08	0.0287	0.0014	8.25E-03
MAY 181215-14 (2)	Hz	Opx	91.0	1.8E-12	1.6E-17	1.4E-15	4.5E-18	1.5E-16	1.5E-09	1.0E-09	1.2E-10	1.2E-12	3.9E-15	4.9E-14	1262.5	35.74	6.70	6.70	0.09	311.7	0.08	0.1785	0.18	9.80	0.13	0.0316	0.0013	4.19E-03
May11-4a	Lh	Opx	91.3	2.2E-11	2.1E-16	4.1E-15	9.4E-18	3.1E-16	3.5E-10	1.3E-09	2.1E-11	6.6E-13	6.5E-16	4.7E-13	5413.7	47.44	6.72	6.72	0.07	1034.9	0.87	0.2010	0.20	10.23	0.09	0.0309	0.0012	3.23E-01
May11-4a (2)	Lh	Opx	91.3	1.1E-12	9.1E-18	2.2E-14	4.5E-17	1.6E-15	3.9E-10	2.8E-09	8.2E-11	1.8E-12	2.6E-15	1.0E-12	49.7	1.08	5.91	5.94	0.14	692.6	0.37	0.1944	0.19	9.99	0.05	0.0296	0.0009	3.49E-03
May11–4b	Hz	Opx	91.0	9.5E-13	8.6E-18	8.0E-15	1.9E-17	6.4E-16	1.2E-09	1.5E-09	–	–	–	–	118.8	–	6.48	6.50	0.09	–	–	–	–	9.95	0.06	0.0308	0.0008	–
May11-4b (2)	Hz	Opx	91.0	4.8E-13	4.4E-18	2.1E-14	4.5E-17	1.5E-15	1.3E-09	2.1E-09	9.3E-11	2.8E-12	2.9E-15	1.9E-12	22.9	0.26	6.44	6.52	0.21	945.3	0.28	0.1963	0.19	9.98	0.04	0.0308	0.0006	1.48E-03
May11-4c	Hz	Opx	91.6	5.5E-11	4.9E-16	2.9E-14	7.5E-17	2.2E-15	6.1E-09	1.8E-09	4.2E-10	3.5E-11	1.3E-14	3.1E-11	1916.6	1.76	6.32	6.32	0.06	2682.3	0.85	0.1990	0.20	10.39	0.02	0.0358	0.0003	3.65E-02
May11-4d	Hz	Opx	91.2	1.1E-11	1.1E-16	9.3E-15	2.2E-17	7.2E-16	3.1E-10	9.1E-10	3.1E-11	1.1E-12	9.8E-16	7.6E-13	1231.7	15.00	6.80	6.81	0.06	1085.2	0.35	0.1788	0.18	10.13	0.04	0.0315	0.0008	1.10E-01
May11-4d (2)	Hz	Opx	91.2	1.0E-12	9.0E-18	2.8E-14	6.0E-17	2.0E-15	2.5E-10	2.3E-09	5.4E-11	1.4E-12	1.7E-15	9.2E-13	36.3	1.10	6.19	6.24	0.18	844.3	0.32	0.2002	0.20	10.07	0.03	0.0314	0.0004	5.27E-03
May11-6a	Hz	Opx	91.2	4.3E-11	4.0E-16	4.4E-14	1.0E-16	3.5E-15	2.7E-07	1.8E-09	7.0E-10	1.1E-11	2.2E-14	4.3E-12	973.9	10.09	6.65	6.66	0.06	494.0	0.07	0.1871	0.19	9.99	0.02	0.0307	0.0003	1.80E-02
May11-6a (2)	Hz	Opx	91.2	5.7E-13	4.4E-18	9.4E-14	2.0E-16	6.8E-15	1.5E-09	1.6E-09	1.2E-09	1.6E-11	3.7E-14	4.7E-12	6.1	–	5.58	5.85	0.20	425.6	0.04	0.1891	0.19	9.92	0.02	0.0306	0.0003	1.19E-04
May11-6a (3)	Hz	Opx	91.2	6.9E-11	5.5E-16	4.5E-14	1.3E-16	4.5E-15	3.0E-07	1.0E-08	1.7E-09	2.4E-11	5.4E-14	8.2E-12	1555.5	8.45	5.86	5.86	0.07	451.7	0.49	0.1812	0.19	9.85	0.02	0.0297	0.0003	1.02E-02
MAY181215-14	Hz	Cpx	92.8	1.5E-12	1.3E-17	2.0E-13	5.9E-16	2.0E-14	3.9E-10	–	7.1E-09	6.6E-11	2.3E-13	–	7.4	–	6.23	6.48	0.10	297.6	0.07	0.1799	0.18	9.83	0.02	0.0297	0.0003	5.65E-05
May11-4a	Lh	Cpx	92.7	2.7E-11	2.5E-16	6.4E-15	1.5E-17	5.0E-16	9.8E-10	1.7E-09	2.2E-11	1.6E-12	6.9E-16	1.4E-12	4163.5	19.35	6.70	6.70	0.06	1909.5	0.00	0.2210	0.22	10.24	0.16	0.0326	0.0013	3.56E-01
May11-4a (2)	Lh	Cpx	92.7	2.6E-12	2.3E-17	5.5E-14	1.2E-16	3.9E-15	–	4.5E-09	2.5E-10	5.7E-12	7.9E-15	3.3E-12	47.1	0.77	6.51	6.55	0.13	725.4	0.24	0.1860	0.18	9.99	0.03	0.0295	0.0007	2.96E-03

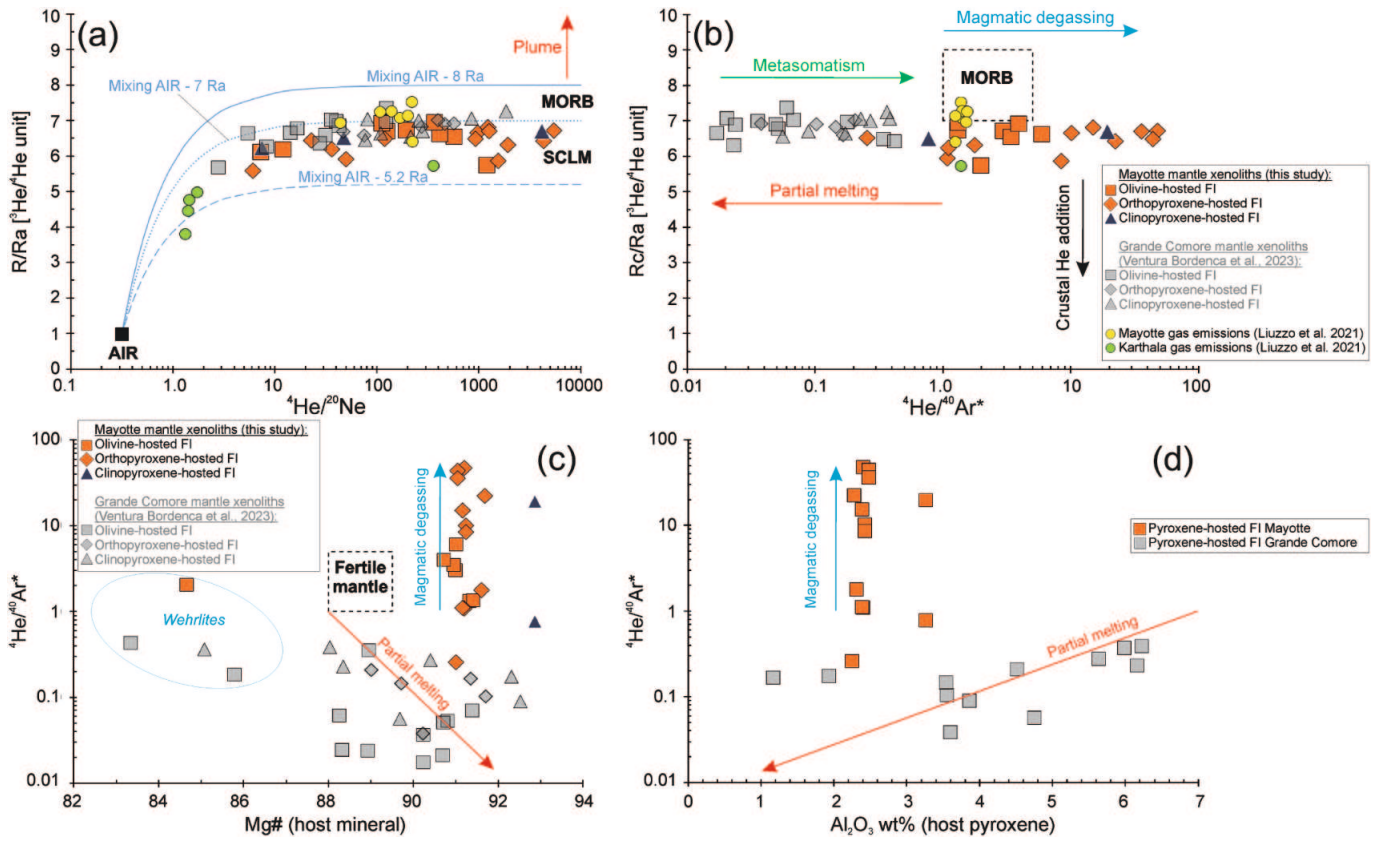

Fig. 5. Chemistry of mineral-hosted fluid inclusions in the ultramafic xenoliths from Petite Terre (Mayotte, this study) and Grande Comore (Ventura Bordenca et al., 2023) measured after single-step crushing compared to the chemistry of surface gas emissions from Mayotte and Karthala volcanoes in Grande Comore (Liuzzo et al., 2021). (a) R/Ra [^{3}He/^{4}He unit] vs. ^{4}He/^{20}Ne ratios. Fields of MORB-like (8 ± 1 Ra; Graham, 2002), SCLM-like (5.2–7.0 Ra; Gautheron and Moreira, 2002; Day et al., 2015; Rizzo et al., 2018, 2021), and plume (>8 Ra) mantle components are also reported. Dashed, dotted and solid lines represent mixing trends between air and SCLM to MORB components, at Ra increasing from 5.2 to 8. (b) Rc/Ra [^{3}He/^{4}He unit] vs. ^{4}He/^{40}Ar* ratios. The dashed field represents the typical MORB-like mantle (8 ± 1 Ra; Graham, 2002), while arrows indicate the main ^{3}He/^{4}He and ^{4}He/^{40}Ar* behaviour during metasomatism, partial melting, magmatic degassing and addition of crustal ^{4}He components (see Rizzo et al., 2021). (c-d) ^{4}He/^{40}Ar* of fluid inclusions vs. host mineral (c) Mg# and (d) Al_2O_3 (wt%) content in ultramafic xenoliths from Petite Terre (Mayotte) (this study) and Grande Comore (Ventura Bordenca et al., 2023). The red arrows indicate the partial melting, while the light blue arrow the magmatic degassing trends (from Rizzo et al., 2021). The dashed field in (c) represents the fertile mantle range of ^{4}He/^{40}Ar* (1–5, Marty, 2012). (For interpretation of the references to colour in this figure legend, the reader is referred to the web version of this article.)

Table 3
Results of 3D volumetric characterization of mineral-hosted fluid inclusions in ultramafic xenoliths from Petite Terre - Mayotte. For each sample, the number of separated grains, their volume, the volume of hosted fluid inclusions and their relative abundance (vol%) are reported. Lh, lherzolite; Hz, harzburgite; Ol, olivine; Opx, orthopyroxene; Cpx, clinopyroxene.

Sample	Rock type	Mineral	Number of analysed grains	Grain volume [μm^3]	Voids volume [μm^3]	Void amount (vol%)
MAY 181215-14	Hz	Ol	20	3.49E+09	3.74E+06	0.11%
MAY 181215-14	Hz	Opx	14	3.46E+09	5.44E+06	0.16%
MAY 181215-14	Hz	Cpx	14	1.86E+09	4.03E+06	0.22%
MAY 11-4a	Lh	Ol	8	4.82E+09	4.59E+06	0.10%
MAY 11-4a	Lh	Opx	9	4.76E+09	1.86E+06	0.04%
MAY 11-4a	Lh	Cpx	4	2.11E+09	2.29E+06	0.11%

depletion with respect to Mayotte mantle xenoliths (Fig. 3a-c-d). This aligns well with the hypothesis of pervasive infiltration of carbonatitic melts/fluids, which induced wehrlitisation of the mantle beneath Grande Comore, replacing orthopyroxene by secondary clinopyroxene characterized by high La/Yb and low Ti/Eu ratios and causing the entrapment of abundant CO_2-rich fluid inclusions (Coltorti et al., 1999; Ventura Bordenca et al., 2023).

The cold and refractory nature of the lithospheric mantle beneath Mayotte is also recorded by thermo-oxybarometric models based on olivine-spinel (Ballhaus et al., 1991 = B91) and orthopyroxene-clinopyroxene (Brey and Köhler, 1990 = BKN90) pairs. Olivine-spinel and orthopyroxene-clinopyroxene thermometry suggests that the Mayotte harzburgites and lherzolites equilibrated in a temperature range from 690 to 870 °C (B91) to 840–980 °C (BKN90), at Δlog fO_2 [FMQ] conditions varying from −1.7 to +0.4 (Fig. S3, S4). The corresponding equilibrium pressure was obtained by two independent methods: i) plotting the olivine-spinel *T* results on the local geotherm (corresponding to 55 mW/m^2, Bessière et al., 2024); ii) using the Ca-in-olivine barometer of Köhler and Brey (1990), the application of which is subordinated to the high-precision determination of Ca content of olivine (see Casetta et al., 2025), allowing for minimization of the uncertainties. Results of the two methods are broadly comparable, as the *P* yielded by plotting the *T* results on the local geotherm range from 1.3 to 1.8 GPa, while the *P* obtained through Ca-in-olivine barometry mostly

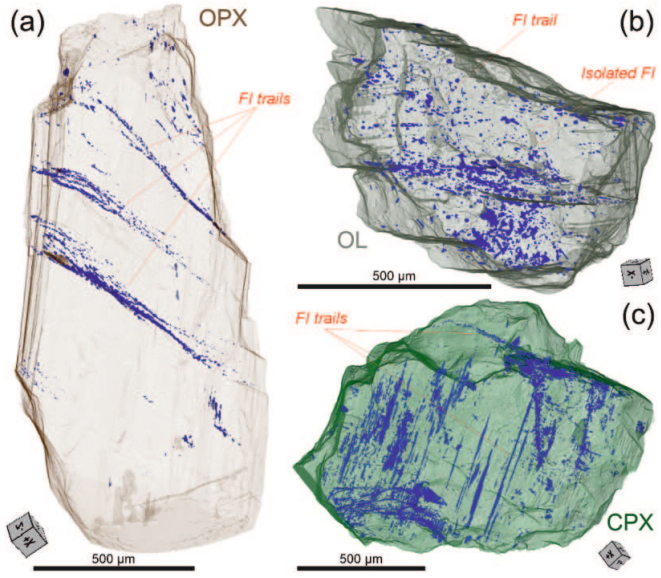

Fig. 6. Volume renderings of an (a) orthopyroxene, (b) olivine and (c) clinopyroxene grains in a harzburgite mantle xenolith from Petite Terre (Mayotte). Scale bar is 500 µm. In all grains, isolated fluid inclusions (FI) and fluid inclusion trails are shown in blue colour. (For interpretation of the references to colour in this figure legend, the reader is referred to the web version of this article.)

clusters at 1.2 to 1.8 GPa, with the exception of a couple of data recording lower *P* (0.7–0.9 GPa) and one yielding a *P* of 2.3 GPa (Table S8). Considering a dP/dZ of 33 MPa/km, the 1.2–1.8 GPa interval of xenoliths equilibrium translates into a depth range of ca. 40–60 km, thus spanning from just above the LAB, located at ~70 km (Feuillet et al., 2021), to the mid-lithosphere. In contrast to Mayotte, mantle xenoliths from Grande Comore yield hotter and slightly more oxidised conditions ($T = 933–1180$ °C; $\Delta \log fO_2$ [FMQ] = −0.9 to +0.7; Ventura Bordenca et al., 2023), confirming the more efficient thermo-chemical perturbation of the lithosphere beneath the western Comores.

Constraints on mantle processes, such as partial melting and metasomatism, can be also extracted from the abundance, isotopic signature of noble gases and key elemental ratios (e.g., $^4He/^{40}Ar^*$, He/CO_2) in mineral-hosted fluid inclusions in ultramafic xenoliths (Rizzo et al., 2018, 2021; Correale et al., 2019; Moreira, 2025). Systematics variations in $^4He/^{40}Ar^*$ and He/CO_2 can be used to discriminate between depleted and fertile lithospheric mantle domains, and to identify the effect of metasomatism, which may locally restore fertile conditions at high or long-lasting melt-rock ratios (Rizzo et al., 2018). This is because He is more incompatible than Ar and CO_2 during mantle melting (Heber et al., 2007; Rosenthal et al., 2015), which means that the progressive melt extraction lowers the $^4He/^{40}Ar^*$ and He/CO_2 ratios of the residual mantle (Rizzo et al., 2018). Fluid inclusions in Grande Comore mantle xenoliths display very low $^4He/^{40}Ar^*$ ratios (0.005–0.4), whereas those in Mayotte mantle xenoliths show significantly higher values (0.3–46.4), partly overlapping and even exceeding the typical mantle production range ($^4He/^{40}Ar^* = 1–5$; Graham, 2002; Marty, 2012) (Fig. 5b). The lack of correlation between $^3He/^4He$ and $^4He/^{40}Ar^*$ in both xenolith populations (Fig. 5b) excludes kinetic fractionation effects due to diffusive He loss (Burnard et al., 2004; Yamamoto et al., 2009), indicating that these differences reflect distinct mantle and/or magmatic processes. In xenoliths from Grande Comore, the extremely low $^4He/^{40}Ar^*$ values (~0.02) measured in olivine-hosted inclusions, overlapping the range of ultra-refractory cratonic mantle domains ($^4He/^{40}Ar^* = 0.0007–0.36$; Correale et al., 2016) are consistent with the extensive partial melting, up to 35%, predating alkaline metasomatism (Ventura Bordenca et al., 2023). The slightly higher values ($^4He/^{40}Ar^* = ~0.4$), mostly observed in pyroxene-hosted inclusions (Fig. 5b), reflect subsequent metasomatism by carbonatitic melt infiltration and wehrlitisation, as also testified by the CO_2 abundance in the fluid inclusions (Ventura Bordenca et al., 2023). The control on fluid inclusions chemistry by partial melting and subsequent metasomatism at Grande Comore is faithfully preserved by the negative correlation between $^4He/^{40}Ar^*$ ratios of fluid inclusions and the Mg# of the host minerals (Fig. 5c) and the positive correlation between the $^4He/^{40}Ar^*$ ratios of fluid inclusions and the Al content of their host pyroxenes (Fig. 5d). Conversely, the $^4He/^{40}Ar^*$ ratios of fluid inclusions at Mayotte (0.3–46.4) are anomalously high and variable when compared to the refractory composition of the xenoliths and do not correlate to the Mg-Al content of the host minerals (Fig. 5c-d), suggesting that their chemistry is not controlled by mantle melting or metasomatism. Indeed, such $^4He/^{40}Ar^*$ ratios are consistent with the values observed in magmatic degassing paths (Fig. 5b) (Burnard et al., 2004; Boudoire et al., 2018; Lo Forte et al., 2024). Their overlap with the $^4He/^{40}Ar^*$ ratios measured in gas emissions from Petite Terre (1.2–1.7) and Karthala (~1.5) (Fig. 5b) further points towards an origin related to magmatic degassing processes. During magmatic degassing, ^{40}Ar is significantly (7–10 times) less soluble than ^4He (and CO_2) and preferentially partitions into the early exsolved gas phase, resulting in initially low $^4He/^{40}Ar^*$ (and He/CO_2) ratios that progressively increase during magma depressurization (Iacono-Marziano et al., 2010; Boudoire et al., 2018). With magma ascent and degassing, the $^4He/^{40}Ar^*$ and He/CO_2 is therefore expected to increase, as documented by olivine-hosted fluid inclusions at Piton de la Fournaise (La Réunion Island) and Fogo volcano (Cape Verde) (Boudoire et al., 2018; Lo Forte et al., 2024). In such a scenario, the high $^4He/^{40}Ar^*$ values (up to ~47) in Mayotte xenoliths could indicate efficient fluid-melt separation and late-stage trapping during the ascent of the host phonolitic magma. This is also suggested by the increase of $^4He/CO_2$ ratios with decreasing CO_2 contents (Fig. S5). The significant overprint of fluids during magma ascent and degassing is also consistent with 3D textural data, which show that fluid inclusions in the different grains of harzburgites and lherzolites are predominantly arranged along trails (Fig. 6), indicating a secondary origin of fluid inclusions and entrapment during brittle deformation of cold, rigid host minerals followed by fracture healing, likely occurring during fluid exsolution from the ascending carrier phonolite magma. The fluid inclusions entrapment during phonolite degassing is also supported by the fact that the highest $^4He/^{40}Ar^*$ values were measured within orthopyroxene and clinopyroxene (Fig. 5b), which, according to the 3D textural data, are the mineral phases hosting dominantly secondary fluid inclusions trails (Fig. 6).

5.2. *Plume vs. lithospheric control on the Comores magmatism*

The presence of a mantle plume beneath the Comores is highly debated. Shear wave tomography data support the existence of a plume (Dongmo Wamba et al., 2023), even though the evidence for a continuous vertical connection from the lower mantle to the surface beneath the Comores is not straightforward as observed beneath the Réunion island. Instead, the low-velocity anomalies imaged beneath the Comores appear to stagnate within the mantle transition zone, suggesting lateral dispersion of plume material rather than direct vertical upwelling. Geochronological data speak against the occurrence of a simple hotspot track with systematic age progression (Rougeau et al., 2025). Although a general westward rejuvenation trend of eruptive products from Mayotte to Grande Comore was proposed (Emerick and Duncan, 1982), recent evidence indicates that the age of volcanism spans from Oligocene-Miocene at Mayotte (~28 Ma) to Pleistocene in submarine products throughout the Mozambique Channel, Pliocene-Holocene in Mohéli (8 ± 2 ka), Anjouan and Grande Comore (Bachèlery and Hémond, 2016; Quidelleur et al., 2022; Rusquet et al., 2023; Boymond et al., 2025; Rougeau et al., 2025), and ultimately to the 2018–2021 eruption at Fani Maoré (Feuillet et al., 2021; Chauvel et al., 2024). Some authors interpret the Comores archipelago as the SE extension of the East African Rift

System (EARS) (Michon, 2015; Famin et al., 2020), due to the coeval magmatism to that of the southern EARS and Madagascar (Berthod et al., 2022). In such frame, the widespread seismo-tectonic activity across the Comores and the concomitant volcanic activity at Karthala (Grande Comore) and Fani Maoré (Mayotte) volcanoes, located at the two opposite sides of the archipelago, would be ascribed to the activity of regional lithospheric structures, causing asthenosphere upwelling and melting along a diffuse plate boundary within the northern Mozambique Channel (Michon, 2015; Famin et al., 2020; Rougeau et al., 2025).

Various geodynamic models have been also proposed to interpret the $^{3}He/^{4}He$ values of volcanic products across the Comores archipelago. The low $^{3}He/^{4}He$ values of olivine-hosted fluid inclusions in Karthala lavas (Fig. 7) were associated to mixing between melts derived from a metasomatized oceanic lithospheric mantle and a low-^{3}He plume (Class et al., 1998, 2005). Conversely, other authors proposed that the $^{3}He/^{4}He$ ratio of fluid inclusions hosted in Grande Comore mantle xenoliths and of surface gas emissions from Grande Comore and Mayotte (5.8–7.5 Ra), do not imply the existence of a mantle plume (Liuzzo et al., 2021; Ventura Bordenca et al., 2023). Volcanic products from Hawaii, having extremely heterogeneous $^{3}He/^{4}He$ ratios (from 7 to 9 up to 16–22 Ra), can be actually produced by a mantle plume, their variability being explained by incorporation, by the plume itself, of filaments of diverse mantle components, including depleted, enriched, and deep-rooted recycled materials (Soltanmohammadi et al., 2021).

In our samples, the distribution of ^{4}He vs Rc/Ra in fluid inclusions (Fig. 7) suggests the absence of diffusive fractionation processes (Burnard et al., 2004; Yamamoto et al., 2009; Rizzo et al., 2018), and confirms that the $^{3}He/^{4}He$ and $^{4}He/^{20}Ne$ ratios, largely insensitive to shallow degassing, can be used to evaluate the magmatic/mantle signature and atmospheric contamination (Fig. 5a, 7). Samples with high $^{4}He/^{20}Ne$ ratios, typically >100, are only marginally affected by atmospheric addition, so that measured $^{3}He/^{4}He$ values closely approach the air-corrected Rc/Ra composition. Fluid inclusions in Mayotte xenoliths have homogeneous Rc/Ra (5.7–6.9), overlapping the values of bubbling gases from Petite Terre (6.4–7.5 Rc/Ra; Liuzzo et al., 2021), those measured in fluid inclusions in Grande Comore mantle xenoliths (6.3–7.4 Rc/Ra; Ventura Bordenca et al., 2023), and in olivine phenocrysts at La Grille volcano, Grande Comore (6.7–7.1 Rc/Ra; Class et al., 2005) (Fig. 5a, 7). By contrast, volcanic products and fumarolic gases from Karthala volcano have systematically lower Rc/Ra both in phenocryst-hosted inclusions (5.0–6.4; Class et al., 2005) and fumaroles (4.7–5.9; Liuzzo et al., 2021) (Fig. 7, S6). Such data suggest that the He isotopic signature of the lithospheric mantle beneath the Comores archipelago is best approximated by the magmatic and mantle products from La Grille and Mayotte (~5.7–7.5 Ra), which cluster between the MORB (7–9 Ra; Graham, 2002) and SCLM-like (5.2–7.0 Ra; Gautheron and Moreira, 2002; Day et al., 2015; Rizzo et al., 2018, 2021) mantle fields (Figs. 5a, 7). Most importantly, the available He-Ne isotopic data across the Comoros archipelago do not provide compelling evidence for a primitive, high-$^{3}He/^{4}He$ plume component, being more consistent with SCLM-MORB-like mantle signatures (Figs. 5a, 7, S6, S7), as documented in other geodynamic settings, such as the European mantle (Rizzo et al., 2018, 2021) or the carbonatitic Oldoinyo Lengai volcano (Tanzania) within the EARS (Sandoval-Velasquez et al., 2025). Framed within the geodynamic evolution of the Mozambique Channel, such results are explainable with the embedding, within the mantle beneath the Comores, of slices of old U-Th-rich SCLM domains, capable of producing a radiogenic ^{4}He ingrowth over time, and do not show evidence of a plume contribution. At a local scale, the $^{3}He/^{4}He$ variability between Mayotte and Grande Comore may reflect differences in sampling depth or their position relative to major lithospheric structures, such as the Davie Fracture Zone, associated with the Jurassic opening of the Mozambique Channel (Phethean et al., 2016; Lemoine et al., 2020). Further support for a predominantly lithospheric control on the Comores magmatism comes from the recent He-Ne-Ar isotopic investigation of submarine glasses from the 2018–2021 Fani Maoré eruption, which revealed MORB-like noble gas signatures ($^{3}He/^{4}He = 6.9 \pm 0.1$ Ra) consistent with low-degree melting of an old, heterogeneous upper mantle promoted by regional extension and edge-driven convection, without requiring a significant chemical contribution from a deep mantle plume (Sauvalle et al., 2026).

5.3. Phonolite genesis and trans-lithospheric degassing beneath Mayotte

Mineral chemistry and *T-P* results show that the Mayotte ultramafic xenoliths represent a portion of a relatively cold ($T < 900$ °C), shallow (40–60 km) and refractory lithospheric mantle (Figs. 2, 3, 6, S1), sampled by the ascending melts without significant thermo-chemical pre-conditioning of the mantle. The 40–60 km depth interval roughly corresponds to the deepest ponding zone of the plumbing system beneath Mayotte volcano (Feuillet et al., 2021), where the ascending basanite melts feeding the 2018–2021 submarine eruption ponded, differentiated, and led to the onset of deep seismicity and to a branching of the magma conduit (Berthod et al., 2021a; Feuillet et al., 2021). To

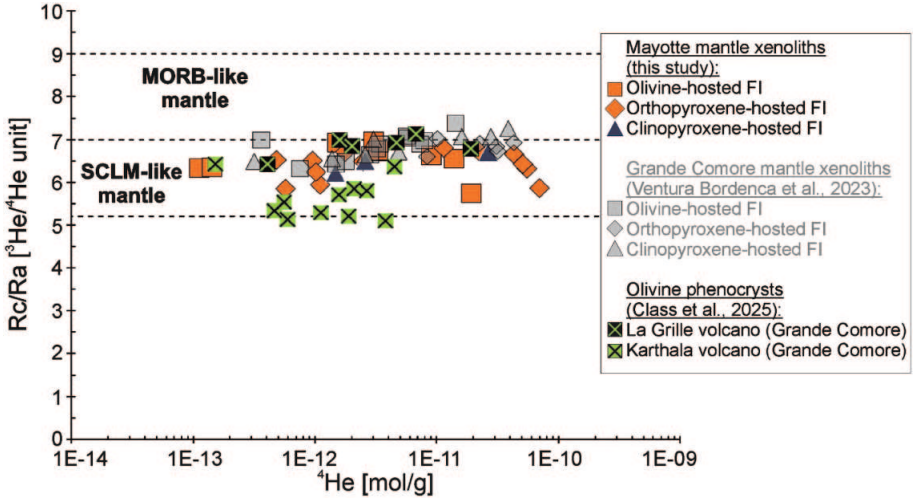

Fig. 7. Rc/Ra ratio [$^{3}He/^{4}He$ corrected for air contamination] vs. ^{4}He [mol/g] in mineral-hosted fluid inclusions in the studied ultramafic xenoliths from Petite Terre (Mayotte) measured after single-step crushing in comparison to those from Grande Comore mantle xenoliths (Ventura Bordenca et al., 2023) and to those in olivine phenocrysts from La Grille and Karthala volcanoes in Grande Comore (Class et al., 2005). The dashed lines indicate the ranges of typical MORB-like (8 ± 1 Ra; Graham, 2002) and SCLM-like (5.2–7.0 Ra; Gautheron and Moreira, 2002; Day et al., 2015; Rizzo et al., 2018, 2021) mantle.

compare the *T-P* conditions of equilibrium recorded by phonolite-hosted mantle xenoliths at Petite Terre to the *T-P* trajectory of evolved basanite melts erupted at Fani Maoré, we applied the newly-refined machine learning thermobarometer (Ágreda-López et al., 2024) to clinopyroxene phenocrysts from the 2018–2021 Fani Maoré eruption (data from Berthod et al., 2021b) and to clinopyroxene grains in the wehrlite cumulate May106 from Petite Terre. The adopted clinopyroxene-only model yields Root Mean Squared Errors of ±57 °C and ± 250 MPa (Ágreda-López et al., 2024). For each input clinopyroxene composition, the algorithm provides the 16th, 50th, and 84th percentiles of the predicted distribution, corresponding respectively to the lower uncertainty bound, the median estimate, and the upper uncertainty bound. These percentiles were used to report asymmetric uncertainties for the calculated *T-P* set of values as 1σ of an asymmetric distribution. Results indicate that the relatively Mg-rich clinopyroxene cores in the Fani Maoré evolved basanites (Mg# = 68–85) started crystallizing at *P* of 1.6 GPa and T of 1203 °C, and continued until 100 MPa and 1053 °C, while the rims (Mg# = 62–82) crystallized in a colder and shallower environment, at *P* < 900 MPa and *T* = 1150–1030 °C (Fig. 8a, Table S9). Clinopyroxene in the cumulate wehrlite carried by phonolites at Petite Terre record *T-P* of last equilibrium of 1149–1171 °C and 0.9–1.2 GPa, comparable to the conditions yielded by clinopyroxene cores in Fani Maoré lavas (Fig. 8a). Within uncertainties, these results provide the evidence that the primary asthenosphere-derived basanite melt, with initial ~2.3 wt% H_2O (Berthod et al., 2021a), ponded and differentiated to phonolites along a trans-lithospheric plumbing system, starting from ~50–60 km of depth beneath both Fani Maoré and Petite Terre (Fig. 8a), in agreement with previous studies (Bachèlery and Hémond, 2016; Berthod et al., 2021a, 2021b).

The studied mantle xenoliths, entrained in a phonolitic host magma, provide a direct constraint on the transport mechanism, and the depth at which phonolites were generated and/or started degassing. The absence of pervasive diffusion/reaction rims around both mantle-derived and cumulate xenoliths (see Berthod et al., 2021b), rules out significant melt-rock interaction during shallow storage or ascent, therefore leading to exclude long-term residence of the xenoliths in a mature ponding zone, like in other oceanic intraplate settings (e.g., Klügel, 1998). Most classical models suggest that phonolite genesis occurs via differentiation at shallow crustal levels (from ~4–6 km to 4–16 km), as observed at the Phlegraean Fields (Italy), Laacher See (Eifel, Germany), or the Dolomites area (Southern Alps, Italy) (Harms et al., 2004; Arienzo et al., 2009; Nardini et al., 2025). However, more recent experimental studies indicate that phonolites can be generated at significantly higher *P* (0.5–1.0 GPa), either via basanite differentiation (Förster et al., 2026) or direct peridotite melting (Laporte et al., 2014). In the case of Mayotte, crystallization experiments and melts modelling showed that phonolites may form in a shallow reservoir at 5–15 to 20 km depth under relatively reduced conditions ($\Delta\log fO_2$ [FMQ] ≈ −1) (Berthod et al., 2021a; Andújar et al., 2023) (Fig. 8c). Our thermobarometric results indicate that the crystallization of clinopyroxene phenocrysts in basanites started at *P* of 1.7 GPa and continued over a broad range of *P*, and that the cumulate wehrlites formed at *P* = 0.9–1.2 GPa (Fig. 8a). This evidence points to the existence of a mature, trans-lithospheric plumbing system, capable of sustaining magma differentiation over a broad depth interval.

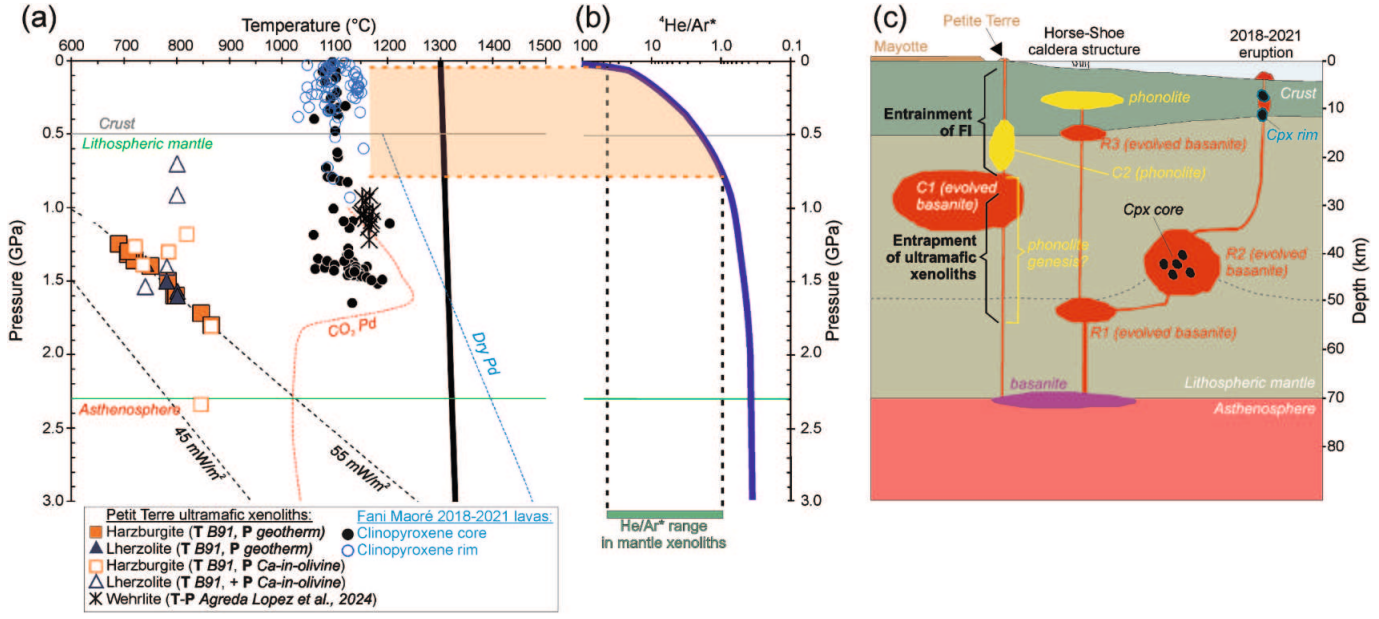

Fig. 8. (a) Pressure (*P*, GPa) vs. temperature (*T*, °C) conditions of last equilibration recorded by the studied harzburgite, lherzolite and cumulate wehrlite xenoliths from Petite Terre (Mayotte). The equilibrium *T* of harzburgite and lherzolite xenoliths were calculated using the olivine-spinel thermometry of Ballhaus et al. (1991), while the equilibrium *P* were calculated by two independent methods: i) plotting the *T* results on the local geotherm (corresponding to 55 mW/m^2, Bessière et al., 2024) - filled symbols; ii) using the Ca-in-olivine barometer of Köhler and Brey (1990) - empty symbols. The equilibrium *T-P* of clinopyroxene grains is the studied cumulate wehrlite sample May106 and in cores and rims of clinopyroxene phenocrysts in 2018–2021 basanites from Fani Maoré (data from Berthod et al., 2021b) are calculated using the machine learning thermobarometric model (Ágreda-López et al., 2024). Black dashed lines represent the 45 and 55 mW/m^2 model geotherms of Hasterok and Chapman (2011). Solidi of dry (Dry Pd) and CO_2-bearing (CO_2-Pd) peridotites (Dasgupta et al., 2013) are also shown. (b) $^4He/^{40}Ar^*$ vs. *P* diagram (as in Lo Forte et al., 2024) showing the degassing trend of fluids in a phonolite melt starting with Ar/He = 0.14 at 1000 °C and 1.5 GPa, calculated using the model of Iacono-Marziano et al. (2010). The $^4He/^{40}Ar^*$ range of most of the studied xenoliths (i.e. 1.0–47 $^4He/^{40}Ar^*$) is shown in the green bar, and translated to *P* of 0.7–0.012 GPa according to the degassing trend shown by the blue curve. (c) Reconstruction of the plumbing system beneath Mayotte, Petite Terre, Horse-Shoe caldera and Fani Maoré (2018–2021 eruption site) based on the thermobarometric results on ultramafic xenoliths, mineral-hosted fluid inclusions (FI) and clinopyroxene phenocrysts in 2018–2021 lavas, in comparison to the previous models. R1, R2 and R3 reservoirs are from Feuillet et al. (2021) and Berthod et al. (2021a, 2021b); the shallow phonolitic reservoir beneath Horse-Shoe is from Andújar et al. (2023); C1 and C2 conductors are from Wawrzyniak et al. (2025). In all panels, location of crust-mantle and lithosphere-asthenosphere boundaries are from Mazzullo et al. (2017), Dofal et al. (2018), Barruol et al. (2019), Berthod et al. (2021a, 2021b), Feuillet et al. (2021) and Wawrzyniak et al. (2025). (For interpretation of the references to colour in this figure legend, the reader is referred to the web version of this article.)

Recent magnetotelluric surveys detected a $> 200\ km^3$ reservoir with high fraction of evolved basanite melt (22–42%) located at minimum depth of 23 km extending from Mayotte to Petite Terre ("Conductor C1"), and a second smaller phonolitic reservoir at 15–20 km depth beneath Petite Terre ("Conductor C2") (Wawrzyniak et al., 2025) (Fig. 8c), Our thermobarometric results suggest that magma differentiation (i.e. cumulate wehrlite production) beneath Petite Terre was efficient already at 0.9–1.2 GPa (27–35 km), and the mantle cargo did not suffer massive shallow re-equilibration, being mostly able to preserve the original *P* of last equilibrium of 1.2–1.8 GPa (35–55 km) (Fig. 8a). Coupled to the textural evidence for absence of reaction rims around the mantle and cumulate xenoliths, and the ability of phonolites to carry peridotite xenoliths with >40 cm diameter during explosive volcanism (Lacombe et al., 2024), our data confirm that the phonolites from Petite Terre reached the surface following a different *T-P* path with respect to the 2018–2021 Fani Maoré eruption (Fig. 8c), and open the question on whether phonolites were generated at crustal levels or possibly in deeper portions of the plumbing system, i.e. within the lithospheric mantle.

In the Petite Terre mantle xenoliths, the occurrence of dominantly secondary fluid inclusions along healed microfractures, as revealed by 3D textural data (Figs. 6, S1, S2), as well as the wide variability in the $^4He/^{40}Ar^*$ and $^4He/CO_2$ ratios and in the CO_2 contents (Figs. 5b, S6), indicate that fluid inclusions were entrapped during mineral cracking, at increasing volatile supersaturation and fluid exsolution in the ascending phonolite host magma. In this framework, the $^4He/^{40}Ar^*$ distribution in fluid inclusions can be used to track the progressive fractionation of volatiles in the fluid phase coexisting with the host phonolite melts during ascent through the lithosphere (Boudoire et al., 2018; Lo Forte et al., 2024; Sandoval-Velasquez et al., 2025). Indeed, the $^4He/^{40}Ar^*$ ratio can be related to pressure estimates, thus providing a quantitative proxy for the depth of fluid entrapment during magma ascent. To retrieve the evolution of $^4He/^{40}Ar^*$ as a function of pressure (Fig. 8b), we assume a fractional equilibrium degassing model, considering a phonolite melt composition typical of Petite Terre (Lacombe et al., 2024) at a broad *T-P* range (800–1000 °C; 0.5–1.5 GPa), for which the solubility model of Iacono-Marziano et al. (2010) yields an initial Ar/He ratio of 0.136–0.146. To anchor the model to the natural dataset, we further assume that the lowest $^4He/^{40}Ar^*$ value measured in olivine-hosted inclusions in xenoliths (~0.4) corresponds to the deepest equilibration conditions in the mantle constrained by xenoliths (~1.8 GPa), while values of $^4He/^{40}Ar^* \approx 1$–2 are representative of near Moho depths (~15–20 km), as observed in other OIB-like systems (Boudoire et al., 2018; Sandoval-Velasquez et al., 2025). Consistently with previous studies in OIB-like settings (Lo Forte et al., 2024), the first exsolved gas phase at volatile saturation has $He/Ar \approx 0.34$ (corresponding to $He/Ar \approx 2.5$ in the parental melt). The degassing trend shows that the $^4He/^{40}Ar^*$ values measured in most xenolith-hosted secondary fluid inclusions (1–47) correspond to the entrapment of fluid exsolved by the host phonolite over a wide *P* interval, from ~0.7 down to ~0.04 GPa (Fig. 8b-c). This indirectly bears witness to the existence of volatiles supersaturated phonolites beneath Petite Terre already at 0.7 GPa. According to our model, the narrow range of $^4He/^{40}Ar^*$ measured in gas emissions at Petite Terre (1.2–1.7) (Fig. 5b; Liuzzo et al., 2021) would correspond to entrapment *P* of ~0.5–0.7 GPa, indicating that present-day surface degassing is produced by melts residing just below the Moho depth, in between the C1 and C2 melt-rich reservoirs identified by magnetotelluric data (Wawrzyniak et al., 2025). Integrating the *P* range recorded by the cumulate wehrlites (0.9–1.2 GPa) to the $^4He/^{40}Ar^*$ modelling, our results show that magma differentiation to phonolite beneath Petite Terre was already efficient at *P* of 0.7–1.0 GPa (Fig. 8c). Yet, the presence of a volumetrically extended reservoir like the C1 Conductor would be expected to cause significant thermo-chemical perturbation of the peridotite mantle, promoting modal metasomatism, melt-rock reactions and diffusion. The cold, refractory and un-metasomatised nature of the peridotite xenoliths, together with the preservation of last equilibrium *P* of 1.2–1.7 GPa and the absence of re-equilibration at shallow depth (except two lherzolite samples, Fig. 8a) allow speculating that the sampling of the xenoliths by the phonolite could have occurred even deeper, i.e., below the C1 reservoir, at $P > 1.2$ GPa. Alternatively, the absence of melt-rock reactions and diffusion can be explained only if the C1 reservoir is partly or entirely composed of already cold phonolite melt (Fig. 8c). In either case, the fluid inclusions record in Mayotte xenoliths enables tracking the continuous degassing trajectory of phonolite melts from the upper lithospheric mantle to shallow crust, and suggests the existence of a mature, trans-lithospheric plumbing system beneath Mayotte.

6. Conclusions

The combined chemical and morpho-textural characterization of minerals and fluid inclusions in phonolite-hosted ultramafic xenoliths from Petite Terre (Mayotte, Comores) provides the opportunity to access information about the nature of the mantle and the deep-seated magma differentiation processes occurring beneath a SiO_2-undersaturated active volcanic system, with implications for both geodynamic and volcano monitoring. The main results of our study are:

1. Harzburgite and lherzolite xenoliths from Petite Terre are fragments of a cold and refractory lithospheric mantle which experienced 20–25% partial melting and re-equilibrated at $T = 690$–870 °C and $P = 0.7$–2.3 GPa. They do not show evidence for significant thermo-chemical perturbation of the lithospheric mantle like the xenoliths from the neighbouring Grande Comore, where alkaline-carbonatitic metasomatism caused wehrlitisation and CO_2 enrichment.
2. The He—Ne isotopic distribution of mineral-hosted fluid inclusions, unaffected by diffusive fractionation, is comparable to that of other volcanic products from the Comores, recording a MORB- to SCLM-like signature of the lithospheric mantle, and not showing evidence for a high-^3He plume component. In such scenario, the EM-like and ^4He-enriched signature of magmas and fumarolic gases at Karthala volcano (Class et al., 2009; Liuzzo et al., 2021) could be explained by dilution of melts with a lithospheric component and/or shallow plumbing system processes.
3. The discrepancy between the $^4He/^{40}Ar^*$ and He/CO_2 in fluid inclusions in ultramafic xenoliths and those in surface gas emissions, and mineral-based thermobarometry on cumulate wehrlite xenoliths vs. phenocrysts in the 2018–2021 eruption confirm the existence of differential *P-T* and degassing trajectories followed by magmas at Petite Terre and Fani Maoré. This implies the existence of a mature, trans-lithospheric plumbing system able to produce deep basanite to phonolite differentiation beneath Petite Terre.
4. The combination of petrographic evidence (i.e., absence of reaction/diffusion coronas) and thermobarometric data confirms that peridotite xenoliths were entrained by phonolites already within the lithospheric mantle and then ascended rapidly to the surface (Lacombe et al., 2024). The $^4He/^{40}Ar^*$ ratios of the dominantly secondary fluid inclusions, ranging in volume from 0.04 to 0.22 vol %, do not correlate to the host mineral chemistry, and record *syn*-degassing fractionation in the host phonolite melts at *P* from 0.7 to 0.004 GPa. Together with the *P* range recorded by the cumulate wehrlites (0.9–1.2 GPa), this data shows that magma differentiation to phonolite beneath Petite Terre was already efficient at *P* of 0.7–1.0 GPa, i.e., in the upper part of the C1 reservoir (Fig. 8c). Alternatively, if we assume that the C1 reservoir beneath Mayotte is hot enough to thermo-chemically perturbate the surrounding lithospheric mantle, then the entrainment of the cold and unreacted peridotite xenoliths by phonolites should have occurred deeper ($P > 1.2$ GPa), indirectly implying that phonolites were generated at a greater depth than previously thought.

CRediT authorship contribution statement

F. Casetta: Writing – original draft, Resources, Investigation, Funding acquisition, Data curation, Conceptualization. **L. Faccincani:** Visualization, Software, Data curation. **A.L. Rizzo:** Writing – review & editing, Validation, Supervision, Software, Methodology, Formal analysis, Data curation. **S. Peres:** Methodology, Data curation. **N. Nardini:** Methodology, Data curation. **B. Faccini:** Methodology, Data curation. **G. Lanzafame:** Software, Methodology, Formal analysis, Data curation. **M. Liuzzo:** Writing – review & editing, Validation, Investigation. **A. Di Muro:** Writing – review & editing, Validation, Supervision, Funding acquisition, Data curation. **M. Prašek:** Software, Methodology, Formal analysis, Data curation. **L. Mancini:** Software, Methodology, Formal analysis, Data curation. **M. Masotta:** Writing – review & editing, Software, Methodology, Formal analysis, Data curation. **F. Colle:** Formal analysis, Data curation. **M. Coltorti:** Writing – review & editing, Supervision, Resources, Project administration, Funding acquisition.

Funding

FC acknowledges funding by the Austrian Science Fund (FWF – Der Wissenschaftsfonds) via the ESPRIT Grant number ESP-605 related to the project "Metasomatism and volatile mobilization in the oceanic mantle", and funding by the Elettra Synchrotron Radiation Facility (Trieste, Italy) via the Project 20230471 "The storage and fingerprint of carbon in Earth's upper mantle". GL acknowledges funding by the Italian Ministry of University and Research (MUR) (CUP E53C24003730001, Project FIS2 "Kinetics of lava flows crystallization"). ALR acknowledges funding by the Italian Minister (Project PRIN2022HA8XCS).

Declaration of competing interest

The authors declare that they have no known competing financial interests or personal relationships that could have appeared to influence the work reported in this paper.

Acknowledgements

The authors thank Franz Kiraly for support during EPMA analyses of thin sections at the University of Vienna (Austria), Giacomo Criniti for support during EPMA analyses of mineral separates at the University of Bayreuth (Germany) and Pier Paolo Giacomoni for support during LA-ICP-MS analyses at the University of Pisa (Italy). We also thank Mariano Tantillo and Mariagrazia Misseri for helping in samples preparation, noble gas analyses and CO_2 extraction from minerals performed at INGV-Palermo (Italy).

The authors thank Tobias P. Fischer for the editorial handling, as well as Azam Soltanmohammadi and an anonymous Reviewer for their thorough and constructive comments on earlier versions of the manuscript.

Appendix A. Supplementary data

Supplementary data to this article can be found online at https://doi.org/10.1016/j.jvolgeores.2026.108785.

Data availability

Data will be made available on request.

References

Ágreda-López, M., Parodi, V., Musu, A., Jorgenson, C., Carfì, A., Mastrogiovanni, F., Petrelli, M., 2024. Enhancing machine learning thermobarometry for clinopyroxene-bearing magmas. Comput. Geosci. 193, 105707.

Andersen, T., Neumann, E.R., 2001. Fluid inclusions in mantle xenoliths. Lithos 55, 301–320.

Andújar, J., Scaillet, B., Moreira, M., Di Carlo, I., Le Friant, A., Bickert, M., Feuillet, N., 2023. Experimental evidence for the shallow production of phonolitic magmas at Mayotte. C. R. Géosci. 354 (S2), 1–32.

Arai, S., 1994. Characterization of spinel peridotites by olivine-spinel compositional relationships: review and interpretation. Chem. Geol. 113 (3–4), 191–204.

Arienzo, I., Civetta, L., Heumann, A., Woerner, G., Orsi, G., 2009. Isotopic evidence for open system processes within the Campanian Ignimbrite (Campi Flegrei–Italy) magma chamber. Bull. Volcanol. 71 (3), 285–300.

Bachèlery, P., Hémond, C., 2016. Geochemical and petrological aspects of Karthala volcano. In: Bachèlery, P., Lénat, J.-F., Di Muro, A., Michon, L. (Eds.), Active Volcanoes of the Southwes tIndian Ocean: Piton de la Fournaise and Karthala. Active Volcanoes of the World. Springer Verlag, Berlin and Heidelberg, pp. 367–384 (Chap. 23).

Baker, D.R., Mancini, L., Polacci, M., Higgins, M., Gualda, G.A.R., Hill, R., Rivers, M., 2012. An introduction to the application of x-ray microtomography to the three-dimensional study of igneous rocks. Lithos 148, 262–276.

Ballhaus, C., Berry, R.F., Green, D.H., 1991. High pressure experimental calibration of the olivine-orthopyroxene-spinel oxygen geobarometer: implications for the oxidation state of the upper mantle. Contrib. Mineral. Petrol. 107 (1), 27–40.

Barruol, G., Sigloch, K., Scholz, J.R., Mazzullo, A., Stutzmann, E., Montagner, J.P., Kiselev, S., Fontaine, F.R., Michon, L., Deplus, C., Dyment, J., 2019. Large-scale flow of Indian Ocean asthenosphere driven by Réunion plume. Nat. Geosci. 12 (12), 1043–1049.

Berthod, C., Komorowski, J.C., Gurioli, L., Médard, E., Bachèlery, P., Besson, P., Lebas, E., 2022. Temporal magmatic evolution of the Fani Maoré submarine eruption 50 km east of Mayotte revealed by in situ sampling and petrological monitoring. C. R. Géosci. 354 (S2), 1–29.

Berthod, C., Médard, E., Bachèlery, P., Gurioli, L., Di Muro, A., Peltier, A., Feuillet, N., 2021a. The 2018-ongoing Mayotte submarine eruption: Magma migration imaged by petrological monitoring. Earth Planet. Sci. Lett. 571, 117085.

Berthod, C., Médard, E., Di Muro, A., Hassen Ali, T., Gurioli, L., Chauvel, C., Komorowski, J.-C., Benbakkar, M., Devidal, J.-L., Besson, P., Le Friant, A., Deplus, C., Nowak, S., Thinon, I., Burckel, P., Hidalgo, S., Feuillet, N., Jorry, S., Fouquet, Y., 2021b. Mantle xenolith-bearing phonolites and basanites feed the active volcanic ridge of Mayotte (Comoros archipelago, SW Indian Ocean). Contrib. Mineral. Petrol. 176 (10), 1–24.

Bessière, E., Poort, J., Cornu, T., Leroy, S., 2024. Heat flow of the Mozambique channel: New data and predicted surface heat flow map. Mar. Pet. Geol. 162, 106723.

Boudoire, G., Di Muro, A., Michon, L., Metrich, N., 2021. Footprints and conditions of multistep alkali enrichment in basaltic melts at Piton de la Fournaise (La Réunion Island, Indian Ocean). Bull. Volcanol. 83 (12), 84.

Boudoire, G., Rizzo, A.L., Di Muro, A., Grassa, F., Liuzzo, M., 2018. Extensive CO_2 degassing in the upper mantle beneath oceanic basaltic volcanoes: first insights from Piton de la Fournaise volcano (La Réunion Island). Geochim. Cosmochim. Acta 235, 376–401.

Boymond, P., Feuillet, N., Thinon, I., Scholtes, L., Zaragosi, S., Leroy, S., Lemoine, A., 2025. En-échelon rifting and origin of the volcanism in the Comoros. Geochem. Geophys. Geosyst. 26 (2), e2024GC011576.

Brey, G.P., Köhler, T., 1990. Geothermobarometry in four-phase lherzolites II. New thermobarometers, and practical assessment of existing thermobarometers. J. Petrol. 31 (6), 1353–1378.

Brun, F., Pacilé, S., Kourousias, G., Dreossi, D., Mancini, L., Tromba, G., Pugliese, R., 2015. Enhanced and flexible software tools for X-ray tomography experiments at the Italian synchrotron radiation facility Elettra. Fundam. Informaticae 141, 233–243.

Burnard, P., Graham, D., Farley, K., 2004. Fractionation of noble gases (he, Ar) during MORB mantle melting: a case study on the Southeast Indian Ridge. Earth Planet. Sci. Lett. 227 (3–4), 457–472.

Casetta, F., Ntaflos, T., Aulbach, S., Ashchepkov, I., Faccincani, L., Abart, R., 2025. The chemical stratigraphy of the sub-cratonic lithospheric mantle and its sampling by kimberlites tracked by olivine trace element content. Chem. Geol. 692, 122969.

Casetta, F., Rizzo, A.L., Faccini, B., Ntaflos, T., Abart, R., Lanzafame, G., Coltorti, M., 2022. CO_2 storage in the Antarctica Sub-Continental Lithospheric Mantle as revealed by intra-and inter-granular fluids. Lithos 416, 106643.

Cashman, K.V., Sparks, R.S.J., Blundy, J.D., 2017. Vertically extensive and unstable magmatic systems: a unified view of igneous processes. Science 355 (6331), eaag3055.

Chauvel, C., Inglis, E.C., Gutierrez, P., Luu, T.H., Burckel, P., Besson, P., 2024. Fani Maoré, a new "young HIMU" volcano with extreme geochemistry. Earth Planet. Sci. Lett. 626, 118529.

Class, C., Goldstein, S.L., Altherr, R., Bachèlery, P., 1998. The process of plume–lithosphere interactions in the ocean basins - the case of Grande Comore. J. Petrol. 39 (5), 881–903.

Class, C., Goldstein, S.L., Shirey, S.B., 2009. Osmium isotopes in Grande Comore lavas: a new extreme among a spectrum of EM-type mantle endmembers. Earth Planet. Sci. Lett. 284 (1–2), 219–227.

Class, C., Goldstein, S.L., Stute, M., Kurz, M.D., Schlosser, P., 2005. Grand Comore Island: a well-constrained "low $^3He/^4He$" mantle plume. Earth Planet. Sci. Lett. 233 (3–4), 391–409.

Coltorti, M., Bonadiman, C., Hinton, R.W., Siena, F., Upton, B.G.J., 1999. Carbonatite metasomatism of the oceanic upper mantle: evidence from clinopyroxenes and glasses in ultramafic xenoliths of Grande Comore, Indian Ocean. J. Petrol. 40 (1), 133–165.

Correale, A., Pelorosso, B., Rizzo, A.L., Coltorti, M., Italiano, F., Bonadiman, C., Giacomoni, P.P., 2019. The nature of the West Antarctic Rift System as revealed by noble gases in mantle minerals. Chem. Geol. 524, 104–118.

Correale, A., Rizzo, A.L., Barry, P.H., Lu, J., Zheng, J., 2016. Refertilization of lithospheric mantle beneath the Yangtze craton in south-East China: evidence from noble gases geochemistry. Gondwana Res. 38, 289–303.
Dasgupta, R., Mallik, A., Tsuno, K., Withers, A.C., Hirth, G., Hirschmann, M.M., 2013. Carbon-dioxide-rich silicate melt in the Earth's upper mantle. Nature 493 (7431), 211–215.
Day, J.M., Barry, P.H., Hilton, D.R., Burgess, R., Pearson, D.G., Taylor, L.A., 2015. The helium flux from the continents and ubiquity of low-$^3He/^4He$ recycled crust and lithosphere. Geochim. Cosmochim. Acta 153, 116–133.
DeVitre, C.L., Wieser, P.E., Bearden, A.T., Richie, A., Rangel, B., Gleeson, M.L., Mulliken, K.M., 2024. Depths in a day - a new era of rapid-response raman-based barometry using fluid inclusions. J. Petrol. 65 (11), egae119.
Dick, H.J., Bullen, T., 1984. Chromian spinel as a petrogenetic indicator in abyssal and alpine-type peridotites and spatially associated lavas. Contrib. Mineral. Petrol. 86 (1), 54–76.
Dofal, A., Fontaine, F.R., Michon, L., Barruol, G., Tkalcic, H., 2018. Crustal structure variation across the southwestern Indian Ocean from receiver functions determined at Ocean-Bottom Seismometers. In: AGU Fall Meeting 2018 abstract T43G0497 (AGU, 2018).
Dongmo Wamba, M., Montagner, J.P., Romanowicz, B., 2023. Imaging deep-mantle plumbing beneath La Réunion and Comores hot spots: Vertical plume conduits and horizontal ponding zones. Sci. Adv. 9 (4), eade3723.
Emerick, C.M., Duncan, R.A., 1982. Age progressive volcanism in the Comores Archipelago, western Indian Ocean and implications for Somali plate tectonics. Earth Planet. Sci. Lett. 60 (3), 415–428.
Faccini, B., Rizzo, A.L., Bonadiman, C., Ntaflos, T., Seghedi, I., Grégoire, M., Coltorti, M., 2020. Subduction-related melt refertilisation and alkaline metasomatism in the Eastern Transylvanian Basin lithospheric mantle: evidence from mineral chemistry and noble gases in fluid inclusions. Lithos 364, 105516.
Famin, V., Michon, L., Bourhane, A., 2020. The Comoros archipelago: a right-lateral transform boundary between the Somalia and Lwandle plates. Tectonophysics 789, 228539.
Feuillet, N., Jorry, S., Crawford, W.C., Deplus, C., Thinon, I., Jacques, E., Van der Woerd, J., 2021. Birth of a large volcanic edifice offshore Mayotte via lithosphere-scale dyke intrusion. Nat. Geosci. 14 (10), 787–795.
Foix, O., Aiken, C., Saurel, J.M., Feuillet, N., Jorry, S.J., Rinnert, E., Thinon, I., 2021. Offshore Mayotte volcanic plumbing revealed by local passive tomography. J. Volcanol. Geotherm. Res. 420, 107395.
Förster, M.W., Prelević, D., Chen, C., Shcheka, S.S., 2026. Lower crustal differentiation and transient shallow assembly of the Laacher See magma system. Lithos 544-545, 108769.
Gautheron, C., Moreira, M., 2002. Helium signature of the subcontinental lithospheric mantle. Earth Planet. Sci. Lett. 199 (1–2), 39–47.
Graham, D.W., 2002. Noble gas isotope geochemistry of mid-ocean ridge and ocean island basalts: Characterization of mantle source reservoirs. Rev. Mineral. Geochem. 47 (1), 247–317.
Harms, E., Gardner, J.E., Schmincke, H.U., 2004. Phase equilibria of the lower Laacher See Tephra (East Eifel, Germany): constraints on pre-eruptive storage conditions of a phonolitic magma reservoir. J. Volcanol. Geotherm. Res. 134 (1–2), 125–138.
Hasterok, D., Chapman, D.S., 2011. Heat production and geotherms for the continental lithosphere. Earth Planet. Sci. Lett. 307 (1–2), 59–70.
Heber, V.S., Brooker, R.A., Kelley, S.P., Wood, B.J., 2007. Crystal–melt partitioning of noble gases (helium, neon, argon, krypton, and xenon) for olivine and clinopyroxene. Geochim. Cosmochim. Acta 71 (4), 1041–1061.
Herman, G.T., 1980. Image Reconstruction from Projections: The Fundamentals of Computerized. Tomography. Academic Press, New York.
Howell, D., Griffin, W.L., Pearson, N.J., Powell, W., Wieland, P., O'Reilly, S.Y., 2013. Trace element partitioning in mixed-habit diamonds. Chem. Geol. 355, 134–143.
Iacono-Marziano, G., Paonita, A., Rizzo, A., Scaillet, B., Gaillard, F., 2010. Noble gas solubilities in silicate melts: new experimental results and a comprehensive model of the effects of liquid composition, temperature and pressure. Chem. Geol. 279 (3–4), 145–157.
Johnson, K.T., 1998. Experimental determination of partition coefficients for rare earth and high-field-strength elements between clinopyroxene, garnet, and basaltic melt at high pressures. Contrib. Mineral. Petrol. 133 (1), 60–68.
Kinzler, R.J., 1997. Melting of mantle peridotite at pressures approaching the spinel to garnet transition: Application to mid-ocean ridge basalt petrogenesis. J. Geophys. Res. Solid Earth 102 (B1), 853–874.
Klügel, A., 1998. Reactions between mantle xenoliths and host magma beneath La Palma (Canary Islands): constraints on magma ascent rates and crustal reservoirs. Contrib. Mineral. Petrol. 131 (2), 237–257.
Köhler, T.P., Brey, G., 1990. Calcium exchange between olivine and clinopyroxene calibrated as a geothermobarometer for natural peridotites from 2 to 60 kb with applications. Geochim. Cosmochim. Acta 54 (9), 2375–2388.
Lacombe, T., Gurioli, L., Di Muro, A., Médard, E., Berthod, C., Bachèlery, P., Komorowski, J.C., 2024. Late Quaternary explosive phonolitic volcanism of Petite-Terre (Mayotte, Western Indian Ocean). Bull. Volcanol. 86 (2), 11.
Lanzafame, G., Peres, S., Casetta, F., Abart, R., Prašek, M., Portale, S., Ferlito, C., 2025. Tracing the pre-to post-eruptive crystallization of trachybasaltic melts: insights into the 1651–1654 CE lavas of Mount Etna (Sicily, Italy). J. Volcanol. Geotherm. Res. 467, 108416.
Laporte, D., Lambart, S., Schiano, P., Ottolini, L., 2014. Experimental derivation of nepheline syenite and phonolite liquids by partial melting of upper mantle peridotites. Earth Planet. Sci. Lett. 404, 319–331.
Le Losq, C., Moretti, R., Médard, E., Berthod, C., Schiavi, F., Trcera, N., Lebas, É., 2026. Oxidation state of Mayotte magmatic series: insights from Fe and S K-edge XANES spectroscopy. Volcanica 9 (2), 481–495.
Lemoine, A., Briole, P., Bertil, D., Roullé, A., Foumelis, M., Thinon, I., Hoste Colomer, R., 2020. The 2018–2019 seismo-volcanic crisis east of Mayotte, Comoros islands: seismicity and ground deformation markers of an exceptional submarine eruption. Geophys. J. Int. 223 (1), 22–44.
Liuzzo, M., Di Muro, A., Rizzo, A.L., Caracausi, A., Grassa, F., Fournier, N., Italiano, F., 2021. Gas geochemistry at Grande Comore and Mayotte volcanic islands (Comoros archipelago), Indian Ocean. Geochem. Geophys. Geosyst. 22 (8), e2021GC009870.
Lo Forte, F.M., Schiavi, F., Rose-Koga, E.F., Rotolo, S.G., Verdier-Paoletti, M., Aiuppa, A., Zanon, V., 2024. High CO_2 in the mantle source of ocean island basanites. Geochim. Cosmochim. Acta 368, 93–111.
Mancini, L., Reinier, E., Cloetens, P., Gastaldi, J., Härtwig, J., Schlenker, M., Baruchel, J., 1998. Investigation of structural defects and inhomogeneities in Al-Pd-Mn icosahedral quasicrystals by combined synchrotron X-ray topography and phase radiography. Phil. Mag. A 78, 1175–1194.
Marty, B., 2012. The origins and concentrations of water, carbon, nitrogen and noble gases on Earth. Earth Planet. Sci. Lett. 313, 56–66.
Mazzullo, A., Stutzmann, E., Montagner, J.P., Kiselev, S., Maurya, S., Barruol, G., Sigloch, K., 2017. Anisotropic tomography around La Réunion island from Rayleigh waves. J. Geophys. Res. Solid Earth 122 (11), 9132–9148.
Melchiorre, M., Faccini, B., Grégoire, M., Benoit, M., Casetta, F., Coltorti, M., 2020. Melting and metasomatism/refertilisation processes in the Patagonian sub-continental lithospheric mantle: a review. Lithos 354, 105324.
Mercier, J.C., Nicolas, A., 1975. Textures and fabrics of upper-mantle peridotites as illustrated by xenoliths from basalts. J. Petrol. 16 (1), 454–487.
Mercury, N., Lemoine, A., Doubre, C., Bertil, D., Van Der Woerd, J., Hoste-Colomer, R., Battaglia, J., 2022. Onset of a submarine eruption east of Mayotte, Comoros archipelago: the first ten months seismicity of the seismo-volcanic sequence (2018–2019). C. R. Géosci. 354 (S2), 105–137.
Michon, L., 2015. The volcanism of the Comoros archipelago integrated at a regional scale. In: Active Volcanoes of the Southwest Indian Ocean: Piton de la Fournaise and Karthala. Springer Berlin Heidelberg, Berlin, Heidelberg, pp. 333–344.
Moreira, M.A., 2025. Noble gases: Tracers of Mantle Dynamics. Structure and Dynamics of the Earth's Interior 1: Dynamics of the Earth's Mantle, p. 187.
Nardini, N., Casetta, F., Ickert, R.B., Tavazzani, L., Okhai, D.C., Peres, S., Coltorti, M., 2025. The timing of the Middle Triassic magmatism in the Dolomites area (Southern Alps, Italy): UPb geochronology of zircon and titanite hosted in plutonic rocks and phonolite dykes. Lithos 494, 107894.
Nougier, J., Cantagrel, J.M., Karche, J.P., 1986. The Comores archipelago in the western Indian Ocean: volcanology, geochronology and geodynamic setting. J. Afr. Earth Sci. (1983) 5 (2), 135–145.
Paganin, D., Mayo, S.C., Gureyev, T.E., Miller, P.R., Wilkins, S.W., 2002. Simultaneous phase and amplitude extraction from a single defocused image of a homogeneous object. J. Microsc. 206 (1), 33–40.
Paton, C., Hellstrom, J., Paul, B., Woodhead, J., Hergt, J., 2011. Iolite: Freeware for the visualisation and processing of mass spectrometric data. J. Anal. At. Spectrom. 26 (12), 2508–2518.
Pearce, J.A., Barker, P.F., Edwards, S.J., Parkinson, I.J., Leat, P.T., 2000. Geochemistry and tectonic significance of peridotites from the South Sandwich arc–basin system, South Atlantic. Contrib. Mineral. Petrol. 139 (1), 36–53.
Pelleter, A.A., Caroff, M., Cordier, C., Bachelery, P., Nehlig, P., Debeuf, D., Arnaud, N., 2014. Melilite-bearing lavas in Mayotte (France): an insight into the mantle source below the Comores. Lithos 208, 281–297.
Phethean, J.J., Kalnins, L.M., van Hunen, J., Biffi, P.G., Davies, R.J., McCaffrey, K.J., 2016. Madagascar's escape from Africa: a high-resolution plate reconstruction for the Western Somali Basin and implications for supercontinent dispersal. Geochem. Geophys. Geosyst. 17 (12), 5036–5055.
Polacci, M., Mancini, L., Baker, D.R., 2010. The contribution of synchrotron X-ray computed microtomography to understanding volcanic processes. J. Synchrotron Radiat. 17, 215–221.
Pouchou, J.L., Pichoir, F., 1991. Quantitative analysis of homogeneous or stratified microvolumes applying the model "PAP". In: Electron Probe Quantitation. Springer US, Boston, MA, pp. 31–75.
Quidelleur, X., Michon, L., Famin, V., Geffray, M.C., Danišík, M., Gardiner, N., Zakaria, M.G., 2022. Holocene volcanic activity in Anjouan Island (Comoros archipelago) revealed by new Cassignol-Gillot groundmass K-Ar and ^{14}C ages. Quat. Geochronol. 67, 101236.
Rizzo, A.L., Faccini, B., Casetta, F., Faccincani, L., Ntaflos, T., Italiano, F., Coltorti, M., 2021. Melting and metasomatism in West Eifel and Siebengebirge Sub-Continental Lithospheric Mantle: evidence from concentrations of volatiles in fluid inclusions and petrology of ultramafic xenoliths. Chem. Geol. 581, 120400.
Rizzo, A.L., Pelorosso, B., Coltorti, M., Ntaflos, T., Bonadiman, C., Matusiak-Małek, M., Bergonzoni, G., 2018. Geochemistry of noble gases and CO_2 in fluid inclusions from lithospheric mantle beneath Wilcza Góra (lower Silesia, Southwest Poland). Front. Earth Sci. 6, 215.
Roedder, E., 1984. Fluid Inclusions. Mineralogical Society of America. Rev. Mineral. 12, 644.
Rosenthal, A., Hauri, E.H., Hirschmann, M.M., 2015. Experimental determination of C, F, and H partitioning between mantle minerals and carbonated basalt, CO_2/Ba and CO_2/Nb systematics of partial melting, and the CO_2 contents of basaltic source regions. Earth Planet. Sci. Lett. 412, 77–87.
Rougeau, S., Quidelleur, X., Famin, V., Michon, L., Nauret, F., Rusquet, A., Di Muro, A., 2025. Reconstruction de l'histoire volcanique de la Grande Comore et implications volcano-tectoniques pour l'archipel des Comores. C. R. Géosci. 357 (G1), 125–144.

Rusquet, A., Famin, V., Quidelleur, X., Michon, L., Nauret, F., Danišík, M., Lemoine, A., 2023. Pliocene-to-Holocene volcano-tectonic activity on Mohéli Island (Comoros archipelago) constrained by new K-Ar ages. J. Volcanol. Geotherm. Res. 442, 107896.

Sandoval-Velasquez, A., Casetta, F., Ntaflos, T., Aiuppa, A., Coltorti, M., Frezzotti, M.L., Rizzo, A.L., 2023b. 2021 Tajogaite eruption records infiltration of crustal fluids within the upper mantle beneath La Palma, Canary Islands. Front. Earth Sci. 12, 1303872.

Sandoval-Velasquez, A., Lages, J., Boudoire, G., Aiuppa, A., Forte, F.L., France, L., Rizzo, A.L., 2025. Evidence of isotopically heavy carbon in the mantle source beneath Oldoinyo Lengai volcano, Tanzania. Chem. Geol. 697, 123126.

Sandoval-Velasquez, A., Rizzo, A.L., Casetta, F., Ntaflos, T., Aiuppa, A., Alonso, M., Pérez, N.M., 2023a. The noble gas signature of the 2021 Tajogaite eruption (La Palma, Canary Islands). J. Volcanol. Geotherm. Res. 443, 107928.

Sauvalle, R., Moreira, M., Scaillet, B., Feuillet, N., Gasser, C., Jorry, S.J., 2026. He-Ne-Ar isotopic constraints on the mantle source of the Fani Maoré paroxysm: Implications for plume involvement beneath the Comoros. Earth Planet. Sci. Lett. 690, 120174.

Schindelin, J., Arganda-Carreras, I., Frise, E., Kaynig, V., Longair, M., Pietzsch, T., Cardona, A., 2012. Fiji: an open-source platform for biological-image analysis. Nat. Methods 9 (7), 676–682.

Soltanmohammadi, A., Grégoire, M., Fontaine, F.J., Bédard, L.P., Blanchard, M., Rabinowicz, M., 2021. Melt percolation, concentration and Dyking in the Hawaiian mantle plume and overriding lithosphere: links to the evolution of lava composition along the volcanic chain. J. Petrol. 63 (1), 1–24.

Sun, S.S., McDonough, W.F., 1989. Chemical and isotopic systematics of oceanic basalts: implications for mantle composition and processes. Geol. Soc. Lond. Spec. Publ. 42 (1), 313–345.

Thivet, S., Hess, K.U., Dingwell, D.B., Berthod, C., Gurioli, L., Di Muro, A., Komorowski, J.C., 2023a. Volatiles of the active Mayotte volcanic chain: STA & EGA-MS analysis of volcanic products. Chem. Geol. 618, 121297.

Thivet, S., Pereira, L., Menguy, N., Médard, É., Verdurme, P., Berthod, C., Troadec, D., Hess, K.U., Dingwell, D.B., Komorowski, J.C., 2023b. Metastable Liquid Immiscibility in the 2018–2021 Fani Maoré Lavas as a Mechanism for Volcanic Nanolite Formation. Commun. Earth Environ. 4 (1), 1–14.

Upton, B.G.J., Downes, H., Kirstein, L.A., Bonadiman, C., Hill, P.G., Ntaflos, T., 2011. The lithospheric mantle and lower crust–mantle relationships under Scotland: a xenolithic perspective. J. Geol. Soc. Lond. 168, 873–885.

Ventura Bordenca, C., Faccini, B., Caracausi, A., Coltorti, M., Di Muro, A., Ntaflos, T., Aiuppa, A., 2023. Geochemical evidence for a lithospheric origin of the Comoros Archipelago (Indian Ocean) as revealed by ultramafic mantle xenoliths from La Grille volcano. Lithos 462, 107406.

Wawrzyniak, P., Gaillard, F., Hautot, S., Andujar, J., Tarits, P., Arbaret, L., Dubois, F., 2025. Magnetotelluric evidence for a melt-rich magmatic reservoir beneath Mayotte. Nature 1–7.

Wieser, P.E., Gleeson, M.L., Rangel, B., DeVitre, C.L., Bearden, A.T., Lynn, K.J., Monteleone, B., 2025. Fluid inclusion constraints on the geometry of the magmatic plumbing system beneath Mauna Loa - part 2: Xenoliths. Bull. Volcanol. 87 (10), 86.

Yamamoto, J., Kurz, M.D., 2023. Noble gas isotopic compositions and abundance ratios of mantle xenoliths from Honolulu series volcanism, Oahu, Hawaii. Earth Planet. Sci. Lett. 603, 117979.

Yamamoto, J., Nishimura, K., Sugimoto, T., Takemura, K., Takahata, N., Sano, Y., 2009. Diffusive fractionation of noble gases in mantle with magma channels: origin of low He/Ar in mantle-derived rocks. Earth Planet. Sci. Lett. 280 (1–4), 167–174.

Zanon, V., Silva, R., Goulart, C., 2023. The crust-mantle transition beneath the Azores region (central-North Atlantic Ocean). Contrib. Mineral. Petrol. 178 (8), 50.